Upper crustal structure and axial topography at intermediate spreading ridges: Seismic constraints from the southern Juan de Fuca Ridge

J. Pablo Canales,[1] Robert S. Detrick,[1] Suzanne M. Carbotte,[2] Graham M. Kent,[3] John B. Diebold,[2] Alistair Harding,[3] Jeffrey Babcock,[3] Mladen R. Nedimović,[2] and Emily van Ark[4]

[1] We use multichannel seismic reflection data to image the upper crustal structure of 0–620 ka crust along the southern Juan de Fuca Ridge. The study area comprises two segments spreading at intermediate rate with an axial high morphology with narrow (Cleft) and wide (Vance) axial summit grabens (ASG). Along most of the axis of both segments we image the top of an axial magma chamber (AMC). The AMC along Cleft deepens from south to north, from 2.0 km beneath the RIDGE Cleft Observatory and hydrothermal vents near the southern end of the segment to 2.3 km at the northern end near the site of the 1980s eruptive event. Along the Vance segment, the AMC also deepens from south to north, from 2.4 to 2.7 km. Seismic layer 2A, interpreted as the basaltic extrusive layer, is 250–300 m thick at the ridge axis along the Cleft segment and 300–350 m thick along the axis of the Vance segment. However, off-axis layer 2A is similar in both segments (500–600 m), indicating ∼90% and ∼60% off-axis thickening at the Cleft and Vance segments, respectively. Half of the thickening occurs sharply at the walls of the ASG, with the remaining thickening occurring within 3–4 km of the ASG. Along the full length of both segments, layer 2A is thinner within the ASG, compared to the ridge flanks. Previous studies argued that the ASG is a cyclic feature formed by alternating periods of magmatism and tectonic extension. Our observations agree with the evolving nature of the ASG. However, we suggest that its evolution is related to large changes in axial morphology produced by small fluctuations in magma supply. Thus the ASG, rather than being formed by excess volcanism, is a rifted flexural axial high. The changes in axial morphology affect the distribution of lava flows along the ridge flanks, as indicated by the pattern of layer 2A thickness. The fluctuations in magma supply may occur at all spreading rates, but its effects on crustal structure and axial morphology are most pronounced along intermediate spreading rate ridges.

1. Introduction

[2] The oceanic crust is created along mid-ocean ridges as plate divergence induces adiabatic mantle upwelling and decompression melting [e.g., *Forsyth*, 1993]. Rising melts accumulate beneath the spreading axis at midcrustal levels [e.g., *Herron et al.*, 1978; *Detrick et al.*, 1987; *Sinton and Detrick*, 1992] (and possibly at deeper levels [e.g., *Kelemen et al.*, 1997; *Dunn et al.*, 2000]) in axial magma chambers (AMC) that are typically narrow (800–1200 m) [*Kent et al.*, 1990] and continuous along axis for tens of kilometers [*Detrick et al.*, 1987]. The upper crust is constructed as magma erupts from the AMC by means of dike injections that generate a sheeted dike complex that has been related to seismic layer 2B and possibly the top of layer 3 [e.g., *Houtz and Ewing*, 1976; *Detrick et al.*, 1994], and ultimately seafloor eruptions that generate a carapace of high-porosity basaltic lavas commonly accepted as forming the seismic layer 2A [e.g., *Herron*, 1982; *Harding et al.*, 1993].

[3] Understanding processes at mid-ocean ridges spreading at intermediate rates (40–90 mm/yr, full rates given hereinafter) is important because they encompass the

---

[1]Department of Geology and Geophysics, Woods Hole Oceanographic Institution, Woods Hole, Massachusetts, USA.
[2]Lamont-Doherty Earth Observatory, Palisades, New York, USA.
[3]Scripps Institution of Oceanography, University of California, San Diego, La Jolla, California, USA.
[4]Massachusetts Institute of Technology-Woods Hole Oceanographic Institution Joint Program, Cambridge, Massachusetts, USA.

transition between two fundamentally different styles of oceanic crustal accretion and lithospheric thermal regimes [e.g., *Small*, 1994; *Ma and Cochran*, 1997]: fast spreading ridges, like the East Pacific Rise (EPR), where larger mantle melting per unit time results in a hotter, weaker axial lithosphere that forms characteristic bathymetric axial highs [e.g., *Phipps Morgan and Chen*, 1993a; *Shah and Buck*, 2001]; and slow spreading ridges, where colder, stronger axial lithosphere results in axial rift valleys [e.g., *Phipps Morgan et al.*, 1987]. At intermediate spreading rates axial morphology is transitional between these end-members, ranging from rifted axial highs, to flat, rough topography, to shallow valleys [e.g., *Hooft and Detrick*, 1995; *Ma and Cochran*, 1996; *Canales et al.*, 1997].

[4] Axial morphology appears to be a major factor controlling lava emplacement on the seafloor. Channelized lava flows are driven by topographic slopes that result in the well-documented, rapid off-axis thickening of the extrusive layer at the EPR [e.g., *Harding et al.*, 1993; *Christeson et al.*, 1994; *Kent et al.*, 1994; *Hooft et al.*, 1996; *Kurras et al.*, 2000; *Fornari et al.*, 2004; *Soule et al.*, 2005]. A study of the intermediate spreading Galápagos Spreading Center (GSC) [*Blacic et al.*, 2004] shows that the amount of off-axis thickening of layer 2A correlates with the along-axis morphological changes resulting from the influence of the nearby Galápagos hot spot [*Canales et al.*, 1997; *Detrick et al.*, 2002; *Sinton et al.*, 2003]. Where the GSC morphology is similar to that of the EPR, layer 2A thickens off-axis considerably. As the axial morphology evolves into a transitional style with wider axial grabens and gentler flank slopes the amount of off-axis thickening of the extrusive layer diminishes and eventually decreases to near zero [*Blacic et al.*, 2004].

[5] Another important characteristic of intermediate spreading ridges is that the depth of the AMC displays a threshold behavior, changing very rapidly from shallow depths (1.2–1.6 km) beneath fast spreading ridges [e.g., *Vera et al.*, 1990; *Kent et al.*, 1994] to 2–4 km deep [*Detrick et al.*, 2002; *Blacic et al.*, 2004; *Baran et al.*, 2005] over a limited range of spreading rates (50–60 mm/yr) for a given magma supply [*Purdy et al.*, 1992; *Phipps Morgan and Chen*, 1993b]. This critical threshold in AMC depth is also accompanied by significant changes in axial morphology. At the GSC, the AMC changes from ~1.5 km depth beneath an axial high to ~2.5–3.0 km depth beneath a transitional morphology over a distance of less than 20 km along the ridge [*Detrick et al.*, 2002; *Blacic et al.*, 2004]. A similar behavior was observed at the intermediate spreading Southeast Indian Ridge (SEIR) [*Cochran et al.*, 1997], where the AMC is shallow (1.5–1.9 km) beneath axial high segments but deeper (2.1–2.3 km) beneath rifted axial highs [*Baran et al.*, 2005].

[6] The above mentioned studies indicate that these observables (axial morphology, AMC depth, and layer 2A thickness) are highly sensitive to subtle variations in magma supply at intermediate spreading rates. Therefore integrating observations of these parameters made at mid-ocean ridges spreading at these critical intermediate spreading rates can shed light on the fundamentals of oceanic crust generation and the linkages between magmatic accretion, hydrothermal circulation, tectonic processes, and seafloor lava emplacement.

[7] To address these problems, we conducted a detailed seismic investigation of the intermediate spreading southern Juan de Fuca Ridge (JdFR). In this paper we show that most of the axis of this spreading center is underlain by a midcrustal reflector that we interpret as the top of the AMC, and that layer 2A thickens off-axis significantly. The correlations we find between axial morphology, AMC depth, and the segment-scale, two-dimensional pattern of layer 2A thickness variation, underline the importance of magma supply variations in controlling the ridge structure at these critical intermediate spreading rates. Our observations also provide constraints on the origin of ridge crest relief and abyssal hill topography at intermediate spreading ridges.

2. Southern Juan de Fuca Ridge: Overview

[8] The JdFR is the boundary between the Pacific and Juan de Fuca plates (Figure 1). Its southern section (full spreading rate of 56 mm/yr [*Wilson*, 1993]) is bounded on the south by the Blanco fracture zone, and it is composed of two major spreading segments that overlap for ~15 km near 45°05′N [*Embley and Chadwick*, 1994]: the Cleft segment (~60 km long) to the south, and the Vance segment (~70 km long) to the north (Figure 1).

2.1. Axial Morphology

[9] In cross section the Cleft segment is a ~20-km-wide elevated axial high (~450 m of relief) with topographic characteristics similar to the EPR near 9°30′N (Figure 2). The main difference is the presence of a 2- to 4-km-wide, ~100-m-deep axial graben-like structure, which is commonly referred to as an "axial valley" in the literature [e.g., *Normark et al.*, 1983]. Because of the connotations that the "axial valley" term has with respect to slow spreading ridges (which typically have valleys several to >10 kilometers wide and several hundreds of meters to >1 km deep [e.g., *Purdy et al.*, 1990]), we prefer to use the term "axial summit graben" (ASG). Along the southern part of the Cleft segment, there is a 50- to 100-m-wide, 5- to 30-m-deep narrow depression or cleft within the ASG that gives the segment its name [*Normark et al.*, 1983, 1986; *Chadwick et al.*, 2001b]. In terms of its dimensions, shape, and volcanic and hydrothermal characteristics, this feature is identical to the axial summit collapse trough (ASCT) found along the EPR [e.g., *Macdonald and Fox*, 1988; *Fornari et al.*, 1998].

[10] To the north, the morphology of the Vance segment has, in general, characteristics similar to those of the Cleft segment. However, the axis of Vance sits on a more subdued axial high (~300 m of relief), and the ASG along Vance is more prominent (6–7 km wide and 200–250 m deep) (Figure 2). Two distinct axial volcanic ridges (AVR) are present within the Vance ASG (Figure 1). To the north of ~45°20′N, the AVR is located east of the center of the ASG [*Applegate*, 1990], while along the southern half of the segment, the AVR is centered in the ASG [*Embley and Chadwick*, 1994].

[11] Features similar to the linear ridges that bound the ASG along both segments can also be observed along the flanks of the southern JdFR, forming a characteristic abyssal hill fabric [e.g., *Kappel and Ryan*, 1986] (Figure 1). *Kappel and Ryan* [1986] explored two possible models for the
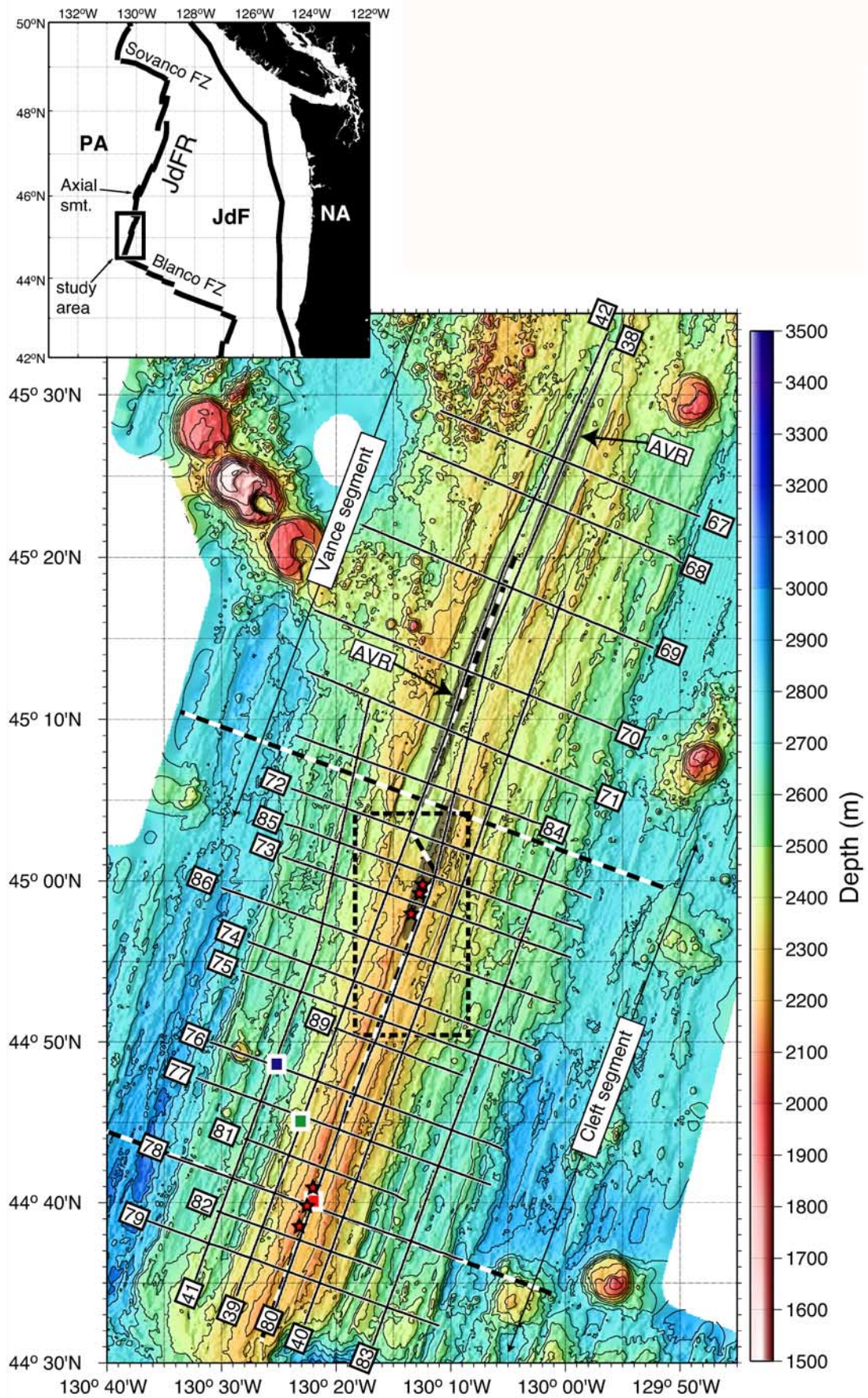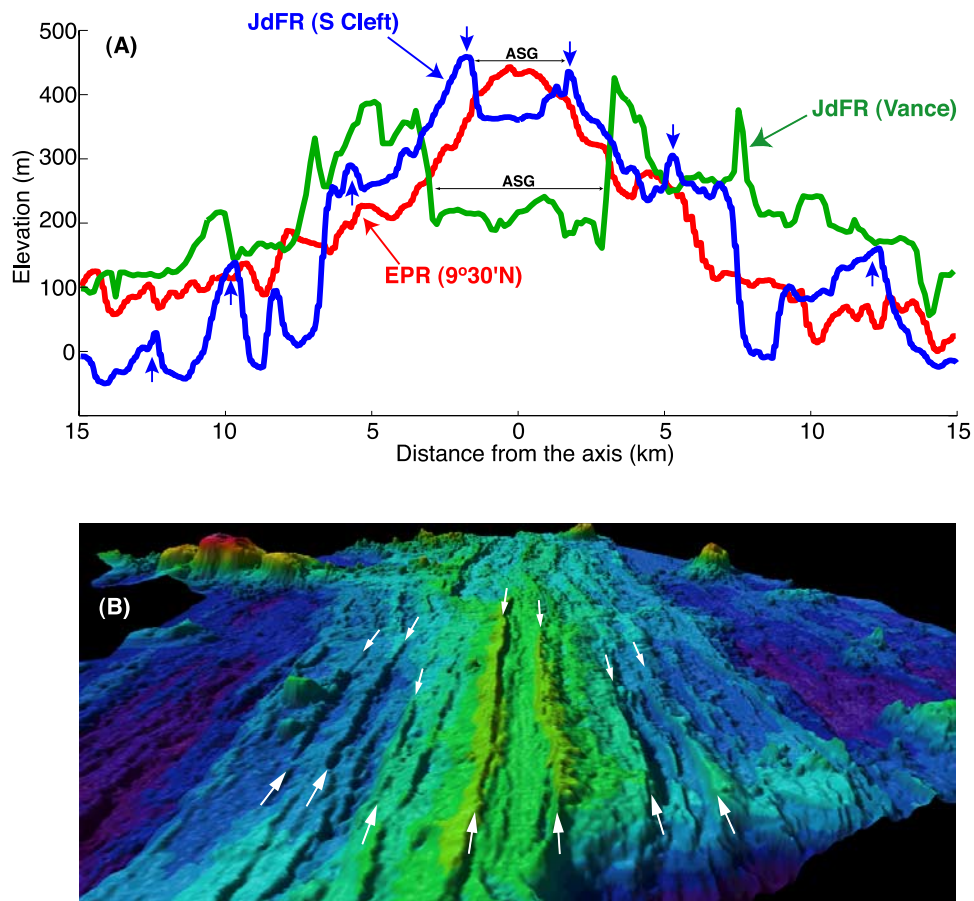
Figure 1

Figure 2. Axial and flank morphology of the southern JdFR. (a) Bathymetry cross sections (single profiles) across the Vance (green) and Cleft (blue) segments and across the East Pacific Rise (red) near 9°30′N. ASG, axial summit graben. (b) Three-dimensional perspective of the study area (view from the SSW, illumination from WNW). Arrows in Figures 2a and 2b point to the present walls of the ASG and some of the abyssal hills that flank the Cleft and Vance segments, interpreted to be shoulders of former ASGs.

origin of these ridges. On the basis of multibeam bathymetry and side-scan sonar records, they favored a nonsteady state model in which the ridges are volcanic constructional highs that formed periodically during times of enhanced volcanism, rather than being steady state features formed by inward facing normal faulting as the crust is carried away from the axis.

2.2. Geological and Petrological Observations

[12] The geology of the Cleft segment has been well studied [e.g., *Normark et al.*, 1983; *Kappel and Ryan*, 1986; *Chadwick and Embley*, 1994; *Embley and Chadwick*, 1994]. The southern part of Cleft is characterized by a young, large sheet flow exhibiting drainage features [*Embley*

and Chadwick, 1994; *Chadwick et al.*, 2001b]. This area hosts high-temperature hydrothermal vents [*Normark et al.*, 1983, 1986] (Figure 1), and it is the site of the RIDGE Cleft Observatory [*Chadwell et al.*, 1999; *Chadwick et al.*, 2001a]. Toward the center of the segment, lavas are older looking and generally more tectonized, typically fractured sheet flows and constructional mounds. The northern part of the segment experienced an eruptive episode in the 1980s [*Chadwick et al.*, 1991], and it is characterized by fresh, glassy sheet flows and pillow mounds, and both high- and low-temperature hydrothermal venting [*Embley et al.*, 1991] (Figure 1).

[13] Basalt samples along the axis of Cleft indicate that there are strong correlations between relative lava age,

Figure 1. Bathymetry map (contours every 100 m) of the Vance and Cleft segments at the southern Juan de Fuca Ridge (JdFR). Numbered solid lines are the multichannel seismic profiles presented in this study. Thick dashed lines correspond to the seismic reflection profiles of *Morton et al.* [1987]. Dashed box corresponds to the seismic refraction study area of *McDonald et al.* [1994]. Red stars show the location of known high-temperature hydrothermal vents, dark gray zone near 45°00′N corresponds to the location of the 1980s eruption, and light gray areas in the Vance segment show the location of the axial volcanic ridges. Red, green, and blue squares show the location of the one-dimensional velocity models of Figures 9 and 10. Top left inset shows the tectonic context of the study area: PA, Pacific plate; JdF, Juan de Fuca plate; NA, North America plate.

Table 1. Processing Sequence and Parameters

Sequence	Steps and parameters
Geometry	CMP gather, 80-fold (6.25 m CMP interval)
Trace editing	
DMO-based suppression of scattered energy	NMO (1500 m/s)
	bottom mute at the primary multiple
	DMO
	f-k dip filter (apparent dips exceeding 2 ms per trace)
	remove NMO (1500 m/s)
Stacking	band-pass filter 5–30 Hz, 12 dB/oct
	velocity analysis every 50–100 CMP
	NMO
	mute (stretch and surgical)
	stack
Time migration	band-pass filter 5–30 Hz, 12 dB/oct
	top mute at the seafloor
	finite difference algorithm [*Lowenthal et al.*, 1976] (maximum dip 5 ms/trace, layer thickness 50 ms)
Display	band-pass filter 5–30 Hz, 12 dB/oct
	top mute at the seafloor and bottom mute at the primary multiple
	exponential gain (24 dB amplitude increase from 0 to 0.5 s below seafloor)

degrees of fractionation, and latitude [*Smith et al.*, 1994], with younger looking and more primitive lavas progressively toward the north [*Smith et al.*, 1994; *Perfit et al.*, 2003]. *Smith et al.* [1994] suggest that lavas were derived from discrete magma lenses, each in different stage of evolution along the axis. Recent mapping, sampling, and submersible observations show that the shoulders of the ASG are capped by moderate to highly evolved lava flows that emanate from ridge-parallel faults and fissures within a disrupted terrain forming the inner face of the ASG walls [*Perfit et al.*, 2003; D. S. Stakes et al., The Cleft revealed: Geologic, magnetic, and morphologic evidence for construction of upper oceanic crust along the southern Juan de Fuca Ridge, submitted to *Geochemistry, Geophysics, Geosystems*, 2005, hereinafter referred to as Stakes et al., submitted manuscript, 2005]. These studies suggest that the evolved off-axis lavas probably erupted from the cooler, distal edges of an axial magma chamber during the end of a magmatic cycle. Within 3 km of the axis there is an apparent increase in age in the lava samples, but the terrain is relatively young looking and is composed of unfaulted constructional features [*Perfit et al.*, 2003].

[14] In contrast to the well-studied Cleft segment, the geology of the Vance segment remains largely unexplored. The detection of a megaplume in the water column in the southern part of the Vance segment in 1987 probably indicates that this part of the segment recently experienced an eruptive event [*Baker et al.*, 1989].

2.3. Geophysical Observations

[15] Despite the large number of geological and petrological observations, few geophysical studies have been conducted at the southern JdFR. Reduced crustal resistivities indicate localized hydrothermal circulation within the upper 1 km of the crust beneath the overlapping spreading axes of Cleft and Vance segments [*Evans et al.*, 1998]. The presence of a crustal magma chamber along the axis of the Cleft and southern Vance segments was first suggested by *Morton et al.* [1987], based on a weak midcrustal reflection observed at depths of 2.3–

2.5 km below the seafloor in seismic reflection profiles (Figure 1).

[16] The structure of the upper crust at the northern Cleft and southern Vance segments from seismic refraction data suggests that the thickness of the extrusive layer (seismic layer 2A) is highly variable (200–550 m), with the thinnest layer 2A located within the ASG of the Cleft segment [*McDonald et al.*, 1994]. A similar pattern was also observed in a magnetic study of the southern JdFR, where an axial magnetic low along Cleft suggests the presence of a thin magnetic source layer within the ASG [*Tivey*, 1994].

3. Seismic Data Acquisition and Processing

[17] In July 2002 we conducted an extensive marine multichannel seismic (MCS) reflection experiment across and along the full length of the JdFR on board the R/V *Maurice Ewing* (cruise EW02-07 [*Carbotte et al.*, 2002]). In this paper we present results from MCS profiles acquired on the Cleft and Vance segments on 0 to ∼620 ka crust (Figure 1). Data were collected along axis-parallel profiles located within the ASG and on the eastern and western flanks of the ridge crest, and along closely spaced across-axis profiles (Figure 1).

[18] The sound source for the MCS survey was a tuned air gun array (10 guns) with a total capacity of 3005 cubic inch (49 L), fired every 37.5 m, and towed at a nominal depth of 7.5 m. Data were collected using a 480-channel Syntron digital streamer with a 6-km-long active section, towed at a nominal depth of 10 m. Data were recorded at a sampling rate of 4 ms in 10.24-s-long records. Accurate locations of shot positions and hydrophone groups were obtained from the ship's Global Positioning System (GPS) and a GPS receiver in the tail buoy at the end of the streamer.

[19] The detailed seismic processing sequence and the parameters used are listed in Table 1. Processing consisted of conventional steps [e.g., *Yilmaz*, 1987] such as sorting to common midpoint (CMP) gathers, trace editing, band-pass filtering, velocity analysis, normal moveout
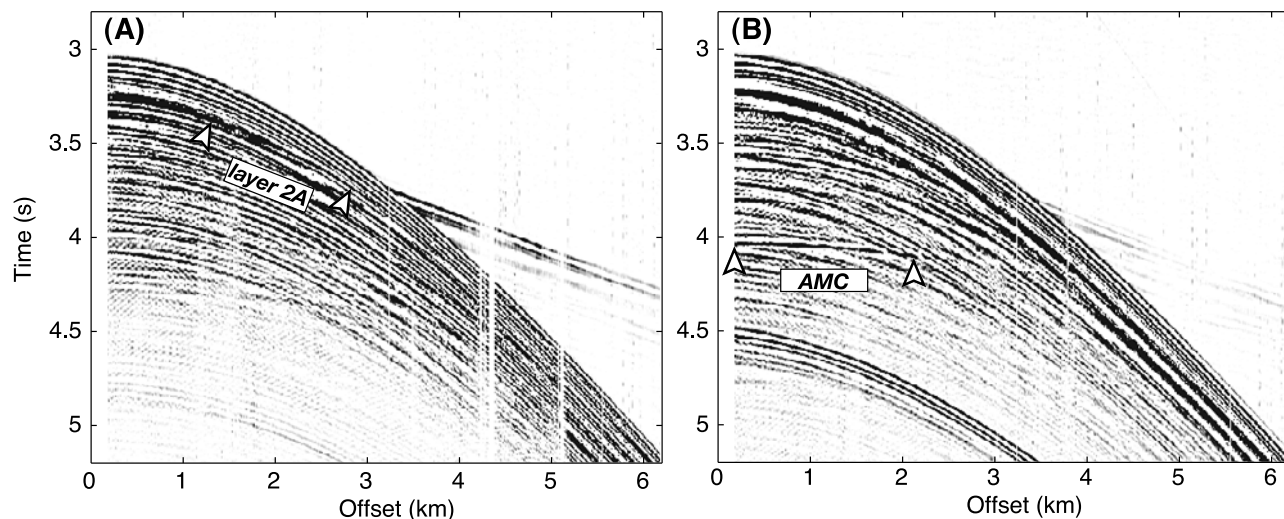
Figure 3. Representative super CMP gathers (constant offset stack composed of 30 consecutive CMP) showing (a) the layer 2A and (b) AMC events.

(NMO) correction, stacking, and migration, and a dip moveout (DMO)-based approach to suppress seafloor-scattered energy [*Kent et al.*, 1996]. This DMO-based filtering (where streamer feathering is minimal) significantly improved the stacked sections since marine seismic data acquired over rough, unsedimented young seafloor is usually contaminated by side echoes and scattered energy. The processing sequence was designed to enhance the stacking of two primary events: the turning energy from the base of layer 2A, which is clearly observed in the CMP gathers within shot-receiver offsets of ~1.3−2.7 km (Figure 3a), and the AMC reflection, observed as a nearly flat event ~1.0 s below the seafloor reflection at 0−2 km offset (Figure 3b).

[20] Figure 4 shows an example of some of the processing steps for line 89 across the center of Cleft segment. The rough topography results in a seismic stack that is highly contaminated by scattered energy, as evidenced by the steeply dipping, crosscutting events (Figure 4a). In this stack the layer 2A event at ~0.3 s below the seafloor is already clear, but the AMC event at ~1 s beneath the spreading axis is degraded by the

scattered energy. The DMO-based filtering removes a significant amount of the scattered energy, making the identification of the AMC event easier (Figure 4b). The final migration results in a sharper image from which layer 2A thickness and AMC depth can be more accurately measured (Figure 4c).

4. Observations

[21] In this section we describe the time-migrated seismic sections. The along-axis profiles provide information on the zero-age thickness of layer 2A and on the presence and depth of the AMC. The across-axis profiles sample 0−620 ka crust and provide constraints on the off-axis thickening of layer 2A and on the width of the AMC. Finally, the flank axis-parallel profiles along 160 ka and 320 ka crust constrain the segment-scale variability of the off-axis layer 2A thickness. Hereinafter, all two-way travel times are reported in seconds below the seafloor. From the migrated images we can confidently pick the base of layer 2A and top of the AMC with an accuracy of 0.04 s and 0.03 s, respectively.
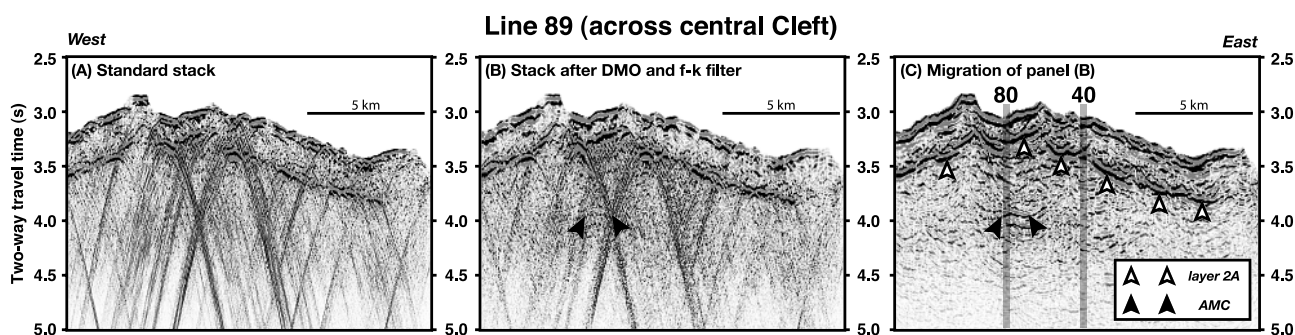

Figure 4. Example of some of the processing steps for line 89. (a) Standard stack. (b) Stack after DMO-based dip filtering. (c) Migration of dip-filtered stack of Figure 4b. White and black arrows indicate the layer 2A and AMC events, respectively. Vertical, numbered gray lines show the crossing points with the across-axis profiles 80 and 40.
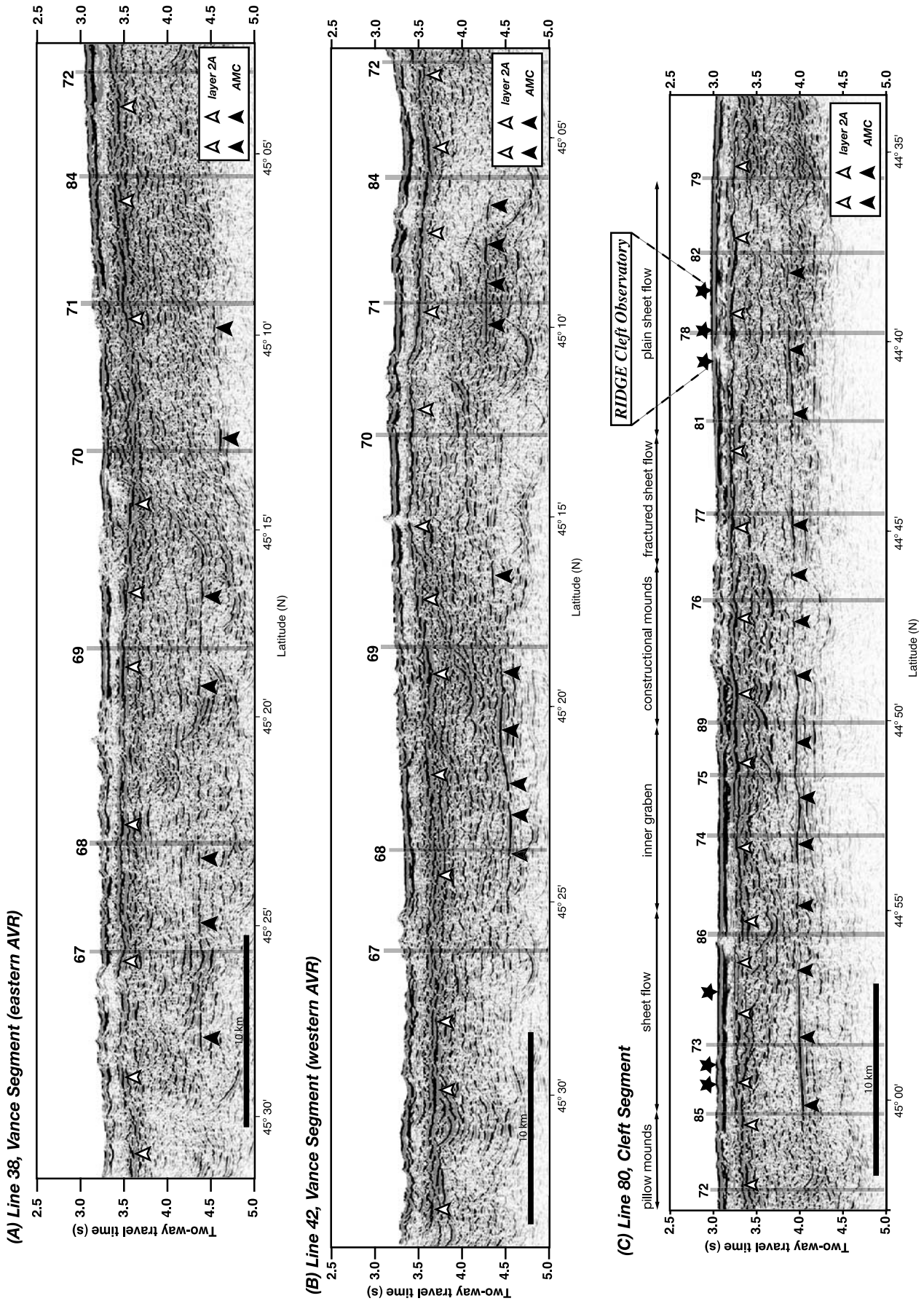
Figure 5

4.1. Vance Segment

4.1.1. Along-Axis Profiles

[22] Two profiles run along the axis of the Vance segment: Line 38 is located over the eastern AVR, and line 42 over the central AVR (Figure 1). The base of layer 2A is well imaged along both profiles (Figures 5a and 5b). Along line 38, the base of layer 2A is generally shallower (0.21–0.27 s) in the northern half of the segment along the eastern AVR, than in the southern half (0.28–0.36 s). The opposite trend is observed along line 42: in the southern part of the segment, along the central AVR, the base of layer 2A is shallower (0.22–0.28 s) than in the northern part (0.28–0.32 s).

[23] A midcrustal reflector interpreted as the top of the AMC is observed along both lines (Figures 5a and 5b). The AMC along line 38 is weak and discontinuous at a depth of 1.06–1.12 s north of 45°15′N. Between 45°15′N and 45°08′N, the AMC is only present along two small, isolated sections (<1 km long) deeper into the crust (1.27–1.31 s). The AMC appears to be better imaged along line 42. It is strong and continuous for ∼10 km between 45°24′N and 45°19′N at 1.11–1.17 s. South of 45°10′N, the AMC is ∼7 km long, and shallower (1.01 s).

4.1.2. Across-Axis Profiles

[24] Six seismic profiles cross the Vance segment between 45°26′N and 45°05′N: lines 67, 68, 69, 70, 71, and 84 (Figure 1). The base of layer 2A is clearly imaged along all of them, both beneath the ASG where it is shallower (0.26–0.34 s), as well as along the flanks of the segment where the base of layer 2A is consistently deeper (0.35–0.4 s) (Figure 6).

[25] With the exception of lines 70 and 84, the AMC is well imaged in the across-axis profiles. The AMC width ranges from 0.6 km at line 68 to 1.7 km at line 69, and the depth is consistent with that observed in the along-axis profiles: 1.05–1.13 s. From these profiles it is clear that only one magma chamber is present beneath the Vance segment at a given latitude. Therefore the different AMC depths observed along lines 38 and 42 at the same latitude (e.g., at 45°10′N, Figures 5a and 5b) are probably consequence of having the streamer misaligned with respect to the top of the AMC along certain parts of the profiles. In other words, in the northern half of the segment line 38 runs along the eastern AVR over the AMC, while line 42 runs to the west of the AMC, imaging (out-of-plane) an apparently deeper AMC. In contrast, along the southern half of Vance segment line 42 runs along the central AVR and over the AMC, while line 38 runs to the east of the AMC, again resulting in an apparently deeper AMC. Thus the AMC along Vance correlates with the location of the AVRs. The AMC shifts, from north to south, from being centered beneath the eastern AVR to being centered beneath the central AVR.

4.2. Cleft Segment

4.2.1. Along-Axis Profiles

[26] Line 80 runs along the center of the Cleft ASG (Figure 1). The base of layer 2a is well imaged along the axis of Cleft at depths of 0.18–0.24 s along the southern half of the segment, moderately increasing up to 0.29 s at the northern end (Figure 5c). A midcrustal reflection attributed to the top of the AMC is clearly present along at least 60% of the axis of Cleft. The depth to the AMC increases from south to north, gently but consistently, from 0.85 s at 44°38′N to 0.94 s at 45°00′N. The AMC is strong and continuous along ∼5- to 10-km-long sections (Figure 5c). Both of the known hydrothermal venting fields near 45°00′N, and at the RIDGE Cleft Observatory near 44°40′N, are underlain by an AMC reflector. The AMC disappears toward both ends of the segment, north of 45°01′N and south of 44°38′N, and it is weaker and less prominent at the center of the segment between 44°46′N and 44°48.5′N. This discontinuity occurs where lava morphology is predominately constructional mounds [Embley and Chadwick, 1994]. However, the cross-axis line 76 shows that the AMC event is present beneath this part of the segment (Figure 7). Therefore the apparent lack of continuity in the AMC beneath the central constructional mounds might be due to poor imaging because of somewhat rougher seafloor, and not a true boundary between two separate magma chambers.

4.2.2. Across-Axis Profiles

[27] Thirteen seismic profiles cross the Cleft segment (Figure 1), which are shown in Figures 4c and 7. As in the case of the Vance segment, the base of layer 2A is shallower beneath the ASG (0.21–0.31 s) than along the flanks of the segment where it is consistently deeper (0.34–0.44 s) (Figure 7). The AMC is apparent in most of the crossing profiles as a narrow (0.6–1.7 km) event beneath the ridge axis at depths of 0.86–0.96 s (Figure 7), consistent with the observations along line 80.

4.3. Flank Axis-Parallel Profiles

[28] Four axis-parallel profiles imaged the crust along the flanks of the Cleft and southern Vance segments (lines 39, 40, 42, and 83, Figure 1). The base of layer 2A is well imaged along the four profiles, at depths of 0.31–0.41 s (Figure 8). We do not find consistent along-axis variations in any of the profiles, or significant differences between the profiles located 4.4 km off-axis (lines 39 and 40) and those located in older crust 9 km away from the axis (lines 41 and 83). There is also not an appreciable difference between the profiles on the eastern and western ridge flanks that could indicate asymmetric crustal accretion by preferential flow of lava toward one side of the axis, as suggested by McDonald et al. [1994].

[29] The axis-parallel profiles are better suited to image the Moho discontinuity, which in these sections is characterized by a weak, very discontinuous low-frequency reflection event at 2.1–2.3 s. This is consistent with the nearly constant subseafloor Moho depth (∼2.3 s) observed in reflection profiles across the flanks of the Cleft segment in 0 to ∼0.7 Ma crust [Nedimović et al., 2005], although from our seismic images it appears that Moho depths are somewhat larger in the southern half of Cleft segment, at least along

Figure 5. Migrated reflection profiles along the axis of Vance and Cleft segments. (a) Line 38, (b) line 42, and (c) line 80. For location, see Figure 1. Vertical, numbered gray lines show the crossing points with the across-axis profiles. White arrows point to our interpretation of the base of layer 2A. Black arrows point to our interpretation of the AMC reflector. Black stars in Figure 5c show the location of high-temperature hydrothermal vents. Lava morphologies along line 80 are from Embley and Chadwick [1994].
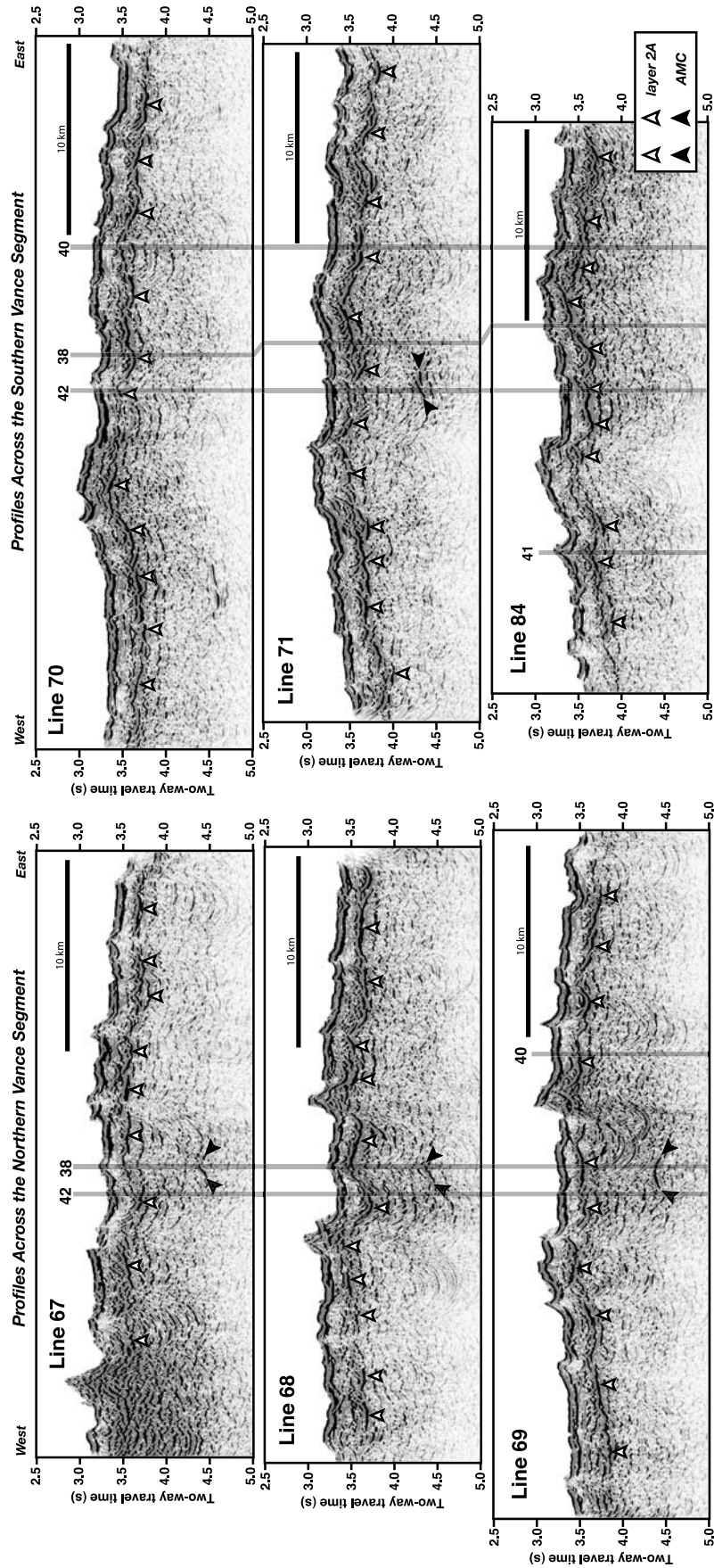
Figure 6. Migrated reflection profiles across the Vance segment. For location, see Figure 1. Symbols are as in Figure 5.
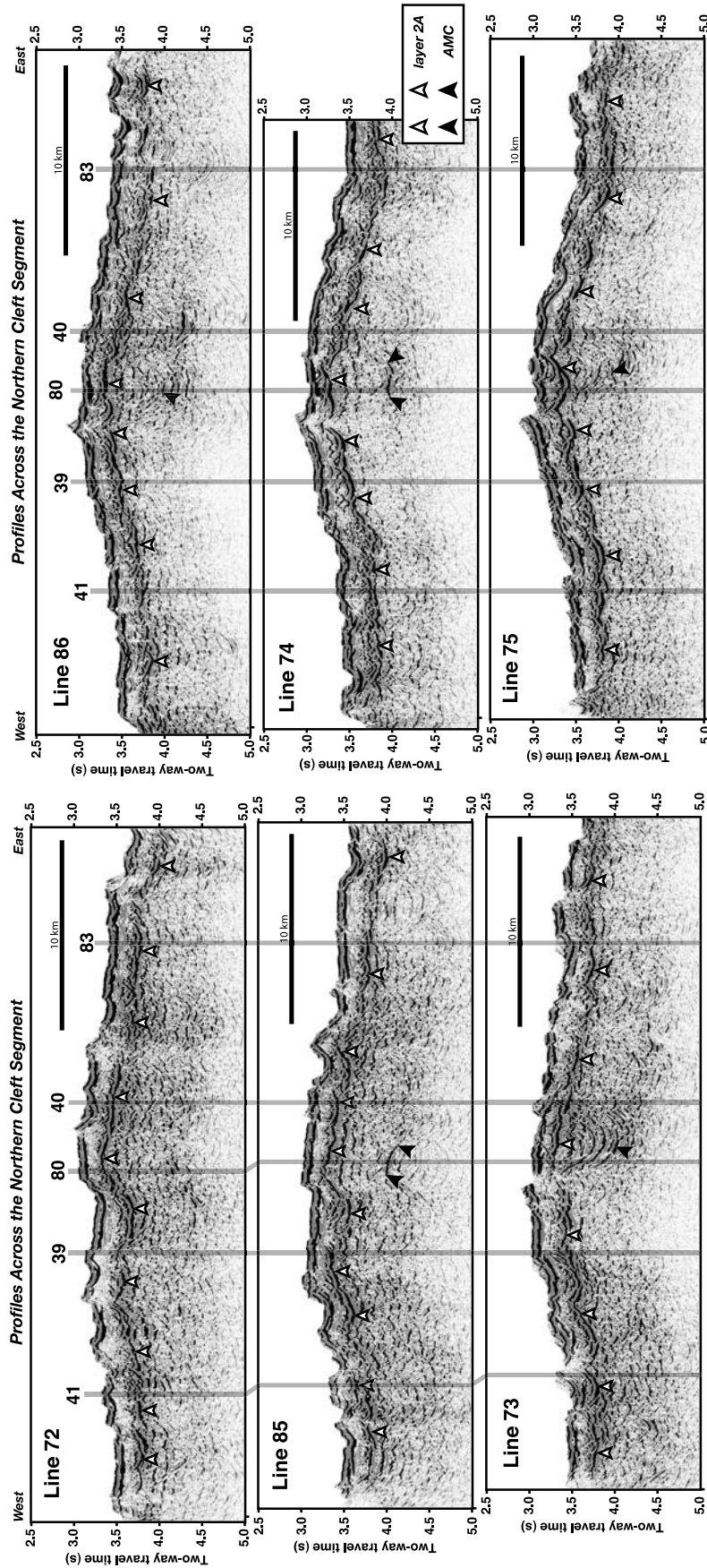
Figure 7. Migrated reflection profiles across the Cleft segment. For location, see Figure 1. Symbols are as in Figure 5.
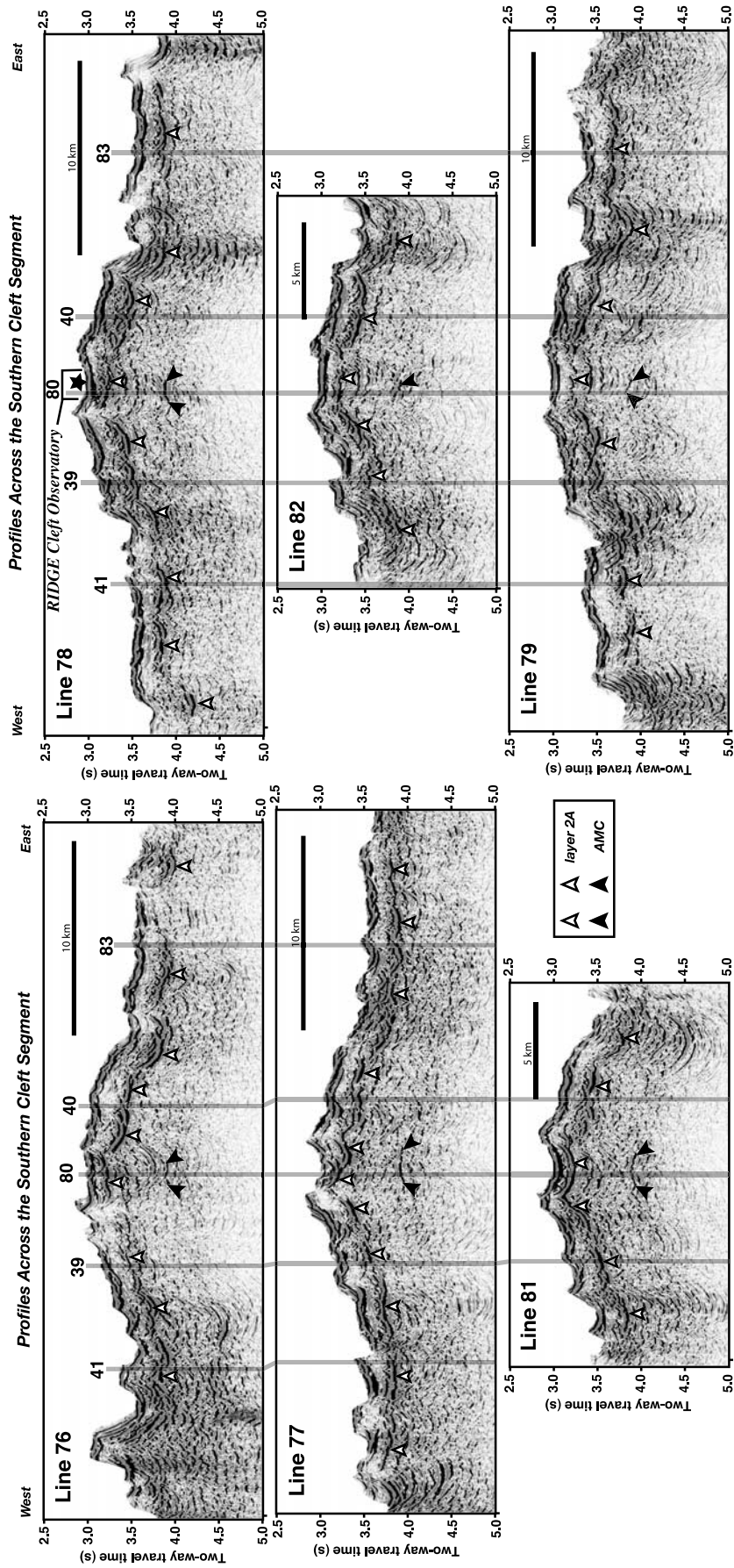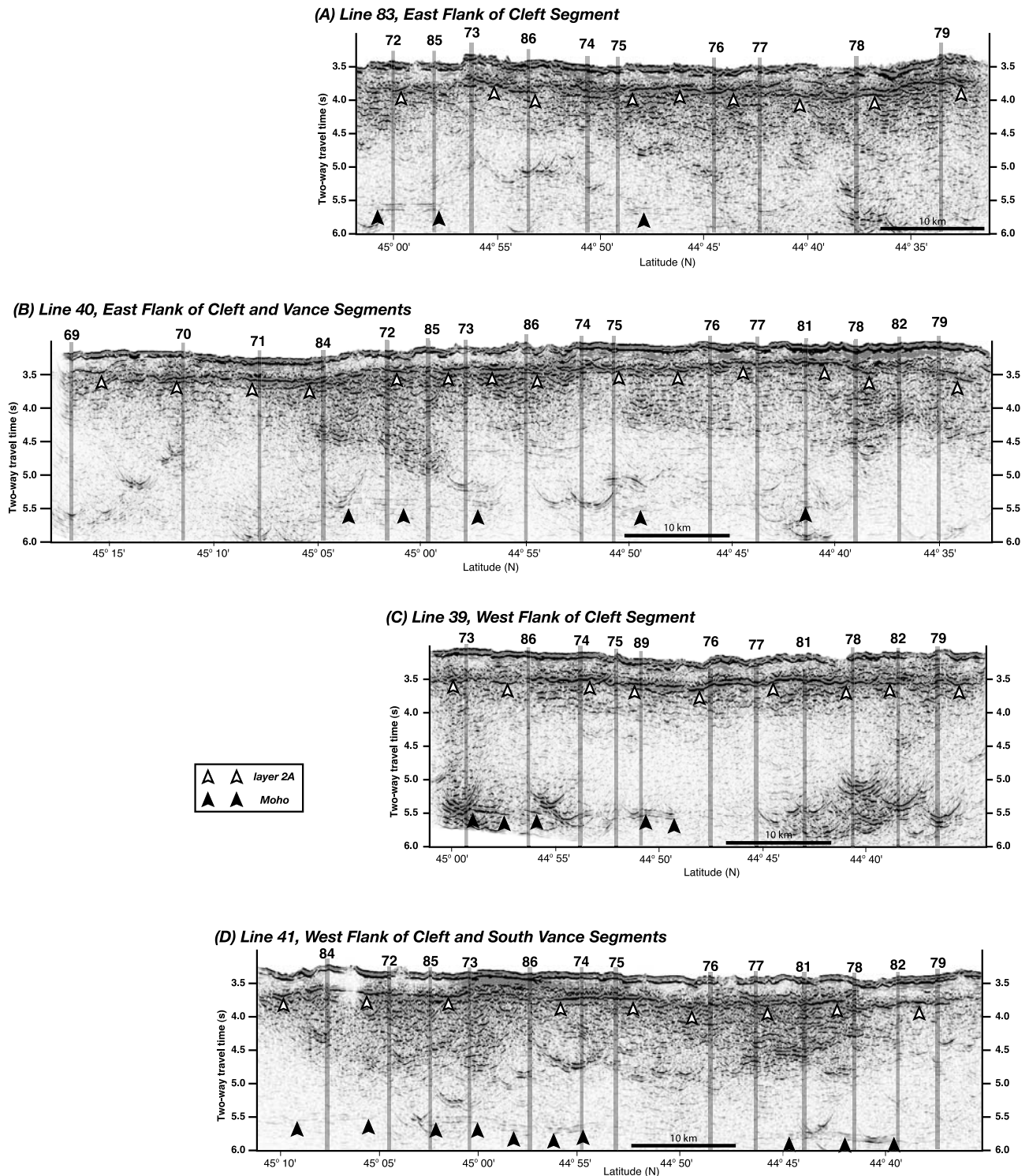
Figure 7. (continued)

Figure 8. Migrated reflection profiles along the flanks of the Cleft and Vance segments. For location, see Figure 1. Symbols are as in Figure 5. Black arrows point to our interpretation of the Moho reflection.

lines 40 and 41 (Figures 8b and 8d). A more detailed study of the Moho in this area is beyond the scope of this paper.

5. Interpretation

5.1. Upper Crustal Seismic Velocity

[30] Our seismic profiles provide information on the depth to the base of layer 2A and top of the AMC as vertical travel time. In order to convert the observed travel times to true layer 2A thickness and AMC depth we need reliable information on the velocity structure of the upper crust. The average upper crustal seismic structure of the northern Cleft segment was estimated by *McDonald et al.* [1994] from seismic refraction data. However, their velocity model might not be valid everywhere in our study area, since upper crustal structure is
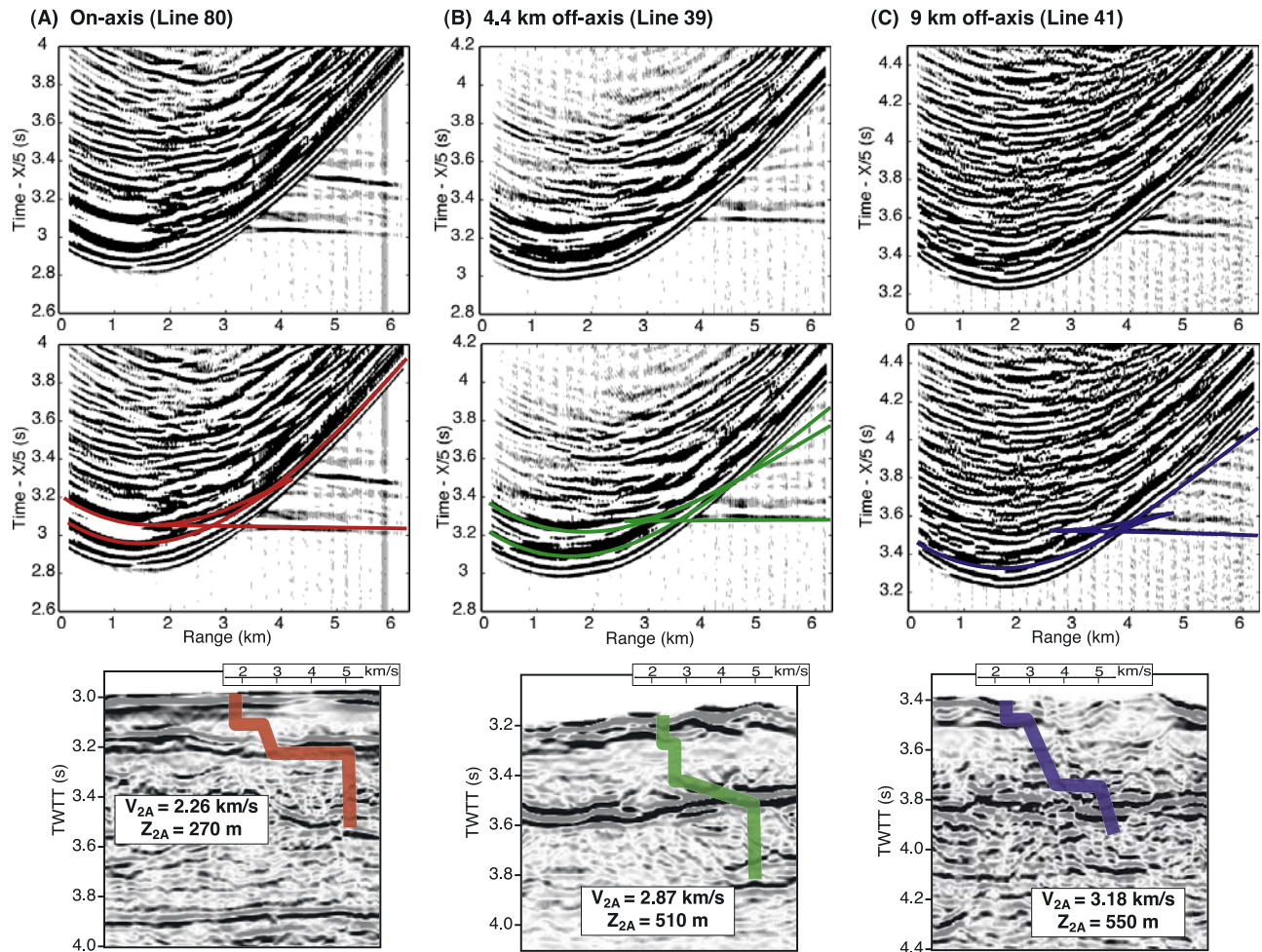
Figure 9. Shot gathers and 1-D velocity models at (a) the axis of Cleft segment (line 80), (b) 4.4 km off axis (line 39), and (c) 9 km off axis (line 41). See location in Figure 1. (top) Shot gather. (middle) Travel times (colored curves) predicted by the velocity models overlaying the observed data. (bottom) Final 1-D velocity models (color lines) overlaying sections of the MCS profiles at the locations of the velocity models, with the average layer 2A velocity and thickness indicated.

strongly age-dependent [e.g., *Grevemeyer and Weigel*, 1996; *Hussenoeder et al.*, 2002]. We have modeled the one-dimensional (1-D) *P* wave velocity structure for the upper ~1 km of the crust at three key locations: on zero-age crust along line 80 at 44°40′N, on 160 ka crust (4.4 km off-axis) along line 39 at 44°45′N, and on 320 ka crust (9 km off-axis) along line 41 at 44°48′N (Figure 1). We have modeled the travel times of layer 2A reflection/refractions and layer 2B refractions observed in shot gathers (Figure 9) using a forward ray-tracing algorithm [*Zelt and Smith*, 1992].

[31] In Figure 9 we show the observed shot gathers as well as the travel times predicted by our models. The final 1-D velocity models are shown in Figure 10. Our velocity models are similar to those of *McDonald et al.* [1994] at the northern Cleft segment and of *Cudrak and Clowes* [1993] at the Endeavour segment in the northern JdFR. One difference with respect to these previous models is that our best fitting models include a velocity step within layer 2A at ~100 m depth (Figure 10). Such structure may be analo-

gous to the base of the surface low-velocity layer of high-porosity lavas and basalt breccia modeled at the EPR [*Christeson et al.*, 1994; *Sohn et al.*, 2004]. However, most importantly, our models provide evidence for the age dependence of the upper crustal structure in this area. On axis, the modeled layer 2A thickness is 270 m, and the interval velocity within layer 2A is 2.26 km/s. At 4.4 km off-axis, layer 2A thickness nearly doubles (510 m), and the interval velocity increases to 2.87 km/s. At the location 9 km off-axis, layer 2A thickness is 550 m, and the interval velocity within layer 2A is 3.18 km/s. In Figure 9 we show that our velocity models are consistent with the seismic reflection profiles by comparing them with the reflection images at the same locations where the 1-D models were obtained. There is an excellent agreement for base of layer 2A between the observed seismic profiles and the modeled structure.

[32] By extrapolating the crustal structure down to the top of the AMC at the on-axis site, we find that the interval velocity above the AMC is 4.7 km/s. Taking into account
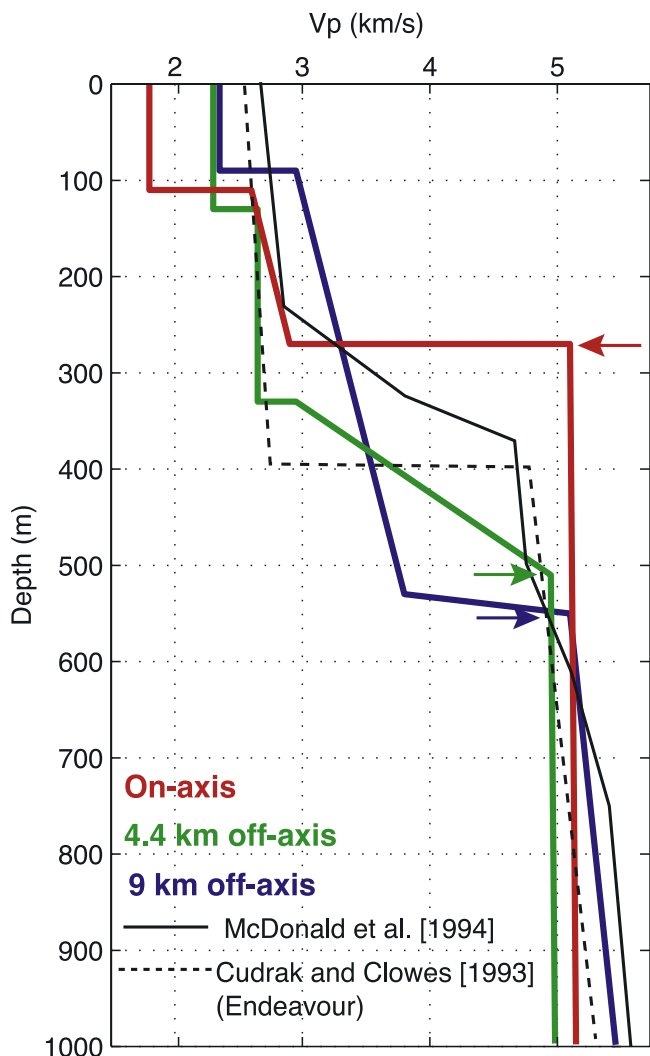
Figure 10. Final 1-D velocity models (colored lines, as in Figure 9) compared to the results of *McDonald et al.* [1994] at the northern Cleft (solid black line), and *Cudrak and Clowes* [1993] at the Endeavour segment in the northern JdFR (dashed line). Arrows point to the base of layer 2A.

both the interval velocities given above, and the uncertainty in the travel time picks for the base of layer 2A and top of the AMC (0.04 s and 0.03 s, respectively), we obtain depth uncertainties of 50–60 m for the on- and off-axis layer 2A

thickness, respectively, and an uncertainty of 70 m for the AMC depth.

5.2. Axial Magma Chamber Geometry

[33] One of the key observations from our data set is the contrasting depth of the AMC between the Cleft and Vance segment, as illustrated in Figure 11, where we show the AMC event for two of the across-axis profiles (line 78 across Cleft and line 69 across Vance). At line 78, the AMC depth is 0.84 s below the seafloor, while at line 69 it is 1.06 s. For an interval velocity of 4.7 km/s, this travel time difference translates into more than a 500 m difference in depth.

[34] At a segment scale, we find that the AMC consistently deepens from the southern end of Cleft to the northern end of Vance (Figures 5 and 12a). The AMC is shallowest (2.0 km) beneath the Cleft Observatory Site and hydrothermal vent field near 44°40′N. From there it deepens gently to 2.3 km at the northern end of Cleft segment, at the site of the 1980s eruptive event and hydrothermal vents near 45°00′N. Further north, the AMC is deeper (2.4 km) at the southern end of Vance, and continues deepening up to 2.7 km near 45°27′N. The previous estimate of AMC depth in this area (2.3–2.5 km [*Morton et al.*, 1987]) is within the range of our observations.

[35] The variation in AMC depth observed in the along-axis profiles is a true geological structure; it is not an artifact due to a possible misalignment of the streamer with respect to the location of the AMC. This is well constrained by the depth to the AMC observed in the across-axis profiles, which are in good agreement with the along-axis observations (Figure 12a). As discussed in section 4.1.2, such misalignment is likely to happen along line 38 in the Vance segment near 45°10′N where the AMC is apparently at 3 km depth because of out-of-plane imaging, while crossing line 71 constrains its true depth at 2.5 km. This is also the case along line 42 near the center of the Vance segment at 45°24′N, where the AMC is apparently at 2.8 km depth but crossing line 68 constrains its true depth at 2.5 km (Figure 12a).

[36] The AMC in Cleft is continuous along ~5- to 10-km-long sections. These variations in AMC amplitude reflect changes in magma chamber properties (e.g., temperature, crystallinity) similar to the variations along the magma chamber at the southern EPR inferred from seismic data [*Singh et al.*, 1998]. Detailed analysis of
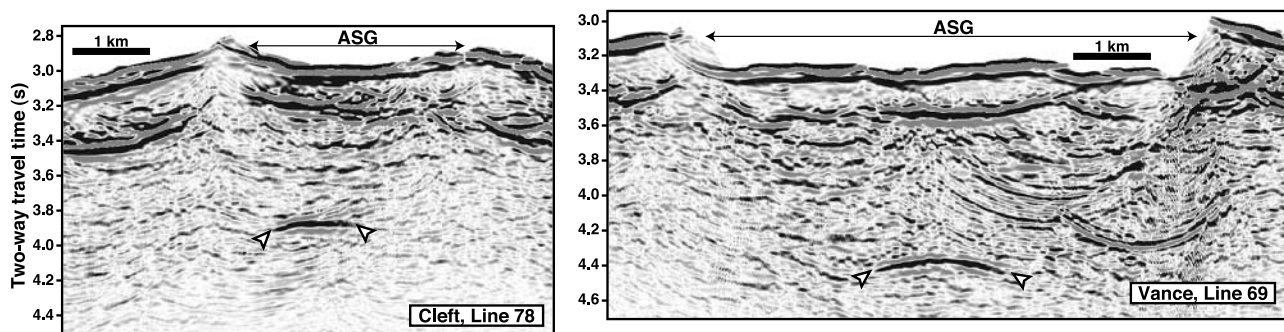

Figure 11. Examples of MCS sections across the Cleft and Vance segment showing the AMC reflector (arrows). Note that both sections are aligned at the seafloor to enhance the difference in AMC depth.
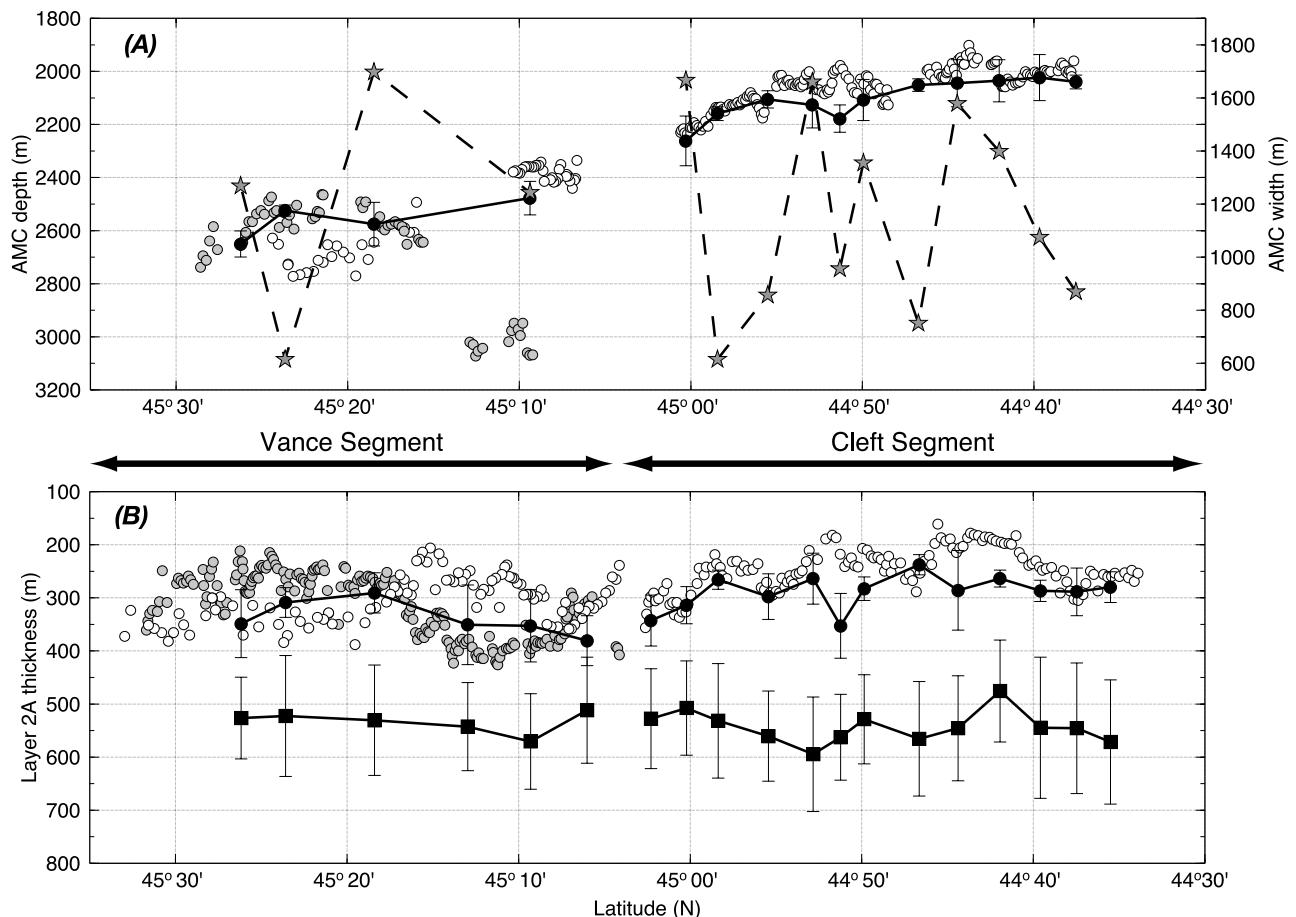
Figure 12. (a) AMC depth versus latitude along the Cleft and Vance segments (left vertical axis). Open circles correspond to measurements along line 80 (Cleft segment) and line 42 (Vance segment). Grey circles correspond to measurements along line 38 (Vance). Solid line and solid circles correspond to the average AMC depth measured in the across-axis profiles (error bars are one standard deviation). Dashed line with grey stars shows the AMC width (right vertical axis) measured in the across-axis profiles. (b) Layer 2A thickness versus latitude along the Cleft and Vance segments. Open circles correspond to measurements along line 80 (Cleft segment) and line 42 (Vance segment). Grey circles correspond to measurements along line 38 (Vance). Solid line with solid circles corresponds to the average layer 2A thickness measured within the ASG in the across-axis profiles (error bars are one standard deviation). Solid line and solid squares correspond to the average layer 2A thickness measured outside the ASG in the across-axis profiles (error bars are one standard deviation).

the seismic properties of the magma chamber at Cleft supports the idea of along-axis changes in crystallinity [*Canales et al.*, 2004], in agreement with the along-axis variation in MgO content of the lavas [*Smith et al.*, 1994]. If replenishment of the AMC from below is not a continuous process, then the AMC at the northern Cleft may still contain a significant amount of melt, while at the southern Cleft the AMC may be mostly crystalline and it may not have yet been replenished after the last eruption. An intriguing aspect, however, is that the deeper section of the AMC along Cleft (northern end) correlates with the more primitive lavas (and therefore higher temperature), while the shallower AMC at the southern Cleft correlates with more evolved lavas probably erupted from a cooler magma chamber. One possible explanation is that the regional crustal thermal regime that controls

the AMC depth (warmer at southern Cleft, cooler at northern Cleft) is related to the magma supply averaged over periods of time longer than the AMC replenishment/eruption cycles, which probably occur at much shorter timescales. In other words, the southern Cleft could still have a somewhat larger melt supply than northern Cleft when averaged over long periods of time, despite being presently less melt rich.

[37] While the AMC events shown in Figure 11 show significant differences in width between the Cleft and Vance segment, we did not find any along-axis trend in AMC width variations, or any correlation between AMC depth and width. The AMC width appears to vary randomly along axis between 0.6 km and 1.7 km (Figure 12a). This variation could be the true nature of the AMC along this portion of the JdFR (although other studies at the GSC

suggest a correlation between AMC depth and width [e.g., *Blacic et al.*, 2004]), or could be due to a combination of suboptimal imaging due to rough seafloor topography, and/ or to the limitation of migration techniques to fully collapse

the energy diffracted at the edges of the AMC [*Kent et al.*, 1990]. Also neither AMC depth or width correlate with lava morphology along the axis of the Cleft segment. Sheet flows at the northern and southern ends of the Cleft
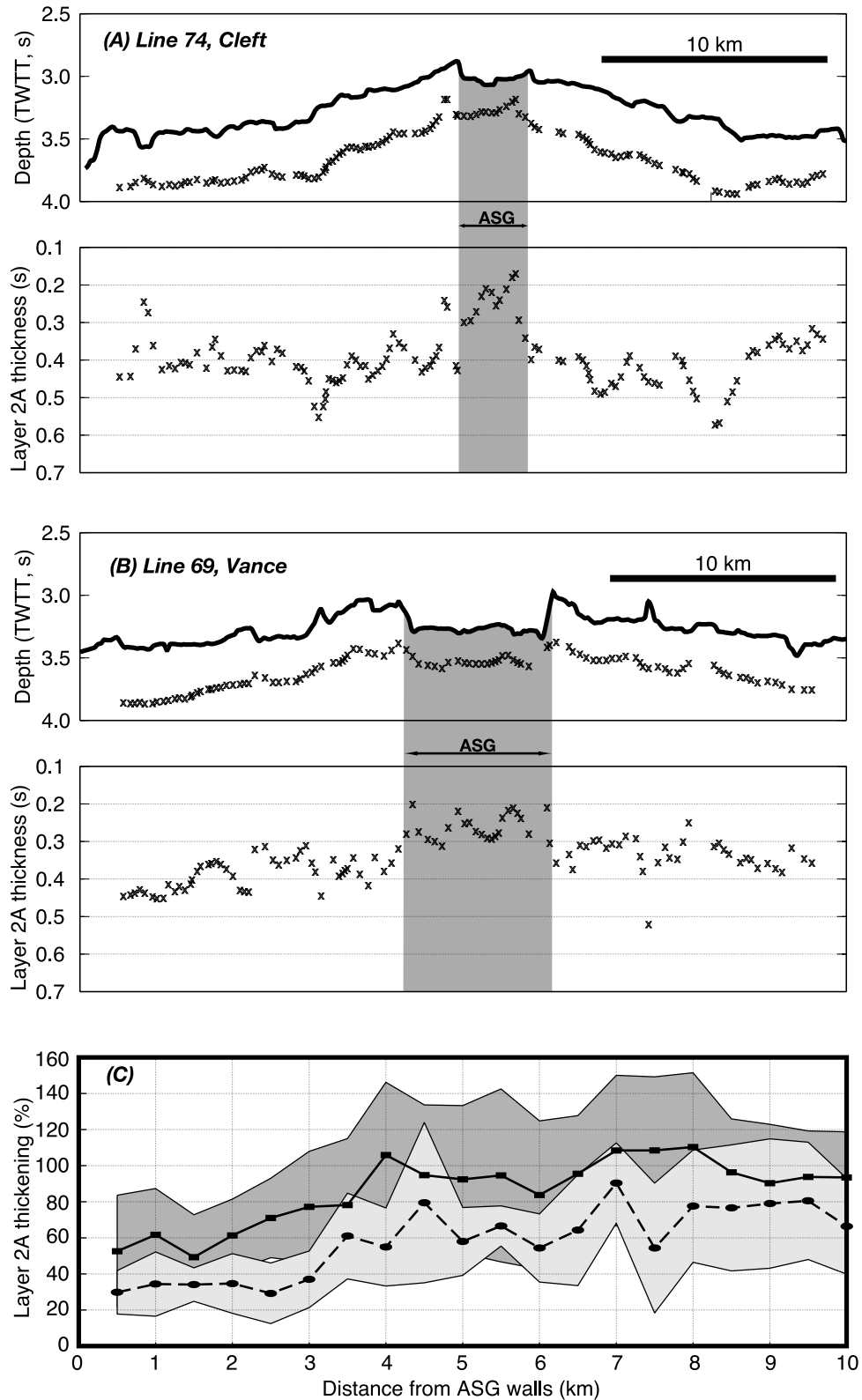

Figure 13

segment are underlain by both, shallower and deeper AMC (Figure 5c).

5.3. Variations in Layer 2A Thickness

[38] We converted the zero-offset two-way travel times to the base of layer 2A observed along all of the migrated profiles using the interval velocities discussed in section 5.1. The layer 2A picks were assigned an interval velocity according to their distance to the ridge axis by linearly interpolating the three velocity models. In Figure 12b we show the on-axis layer 2A thickness measured both in the along-axis profiles and in the across-axis profiles as average values inside the ASG. On average, on-axis layer 2A thickness along the Cleft segment is nearly constant (250–300 m), with a slight increase at the north end of the segment toward the overlapping zone between Cleft and Vance. There is no clear correlation between layer 2A thickness and lava morphology along the axis of the Cleft segment. Along the Vance segment, on-axis layer 2A thickness is somewhat larger (300–350 m), and also appears to increase toward the overlapping zone between 45°00′N and 45°10′N.

[39] We find a remarkable difference between the on-axis layer 2A thickness and the off-axis thickness outside the ASG (Figure 12b). Averaged off-axis layer 2A thickness remains relatively constant along both the Cleft and Vance segments: 500–600 m. This indicates that layer 2A thickness increases off-axis by ~90% and ~60% along the flanks of Cleft and Vance segments, respectively. Note that the difference in percentage of layer 2A thickening between the Cleft and Vance segments is due to their different on-axis layer 2A thickness; the off-axis thickness is the same for both segments. In Figure 13 we show two profiles across the Cleft and Vance segment showing layer 2A thickness, axial topography, and width of the ASG. It is evident that in both cases a significant amount of the layer 2A thickening occurs sharply, immediately at the bounding walls of the ASG. Figure 13c shows the averaged increase in off-axis layer 2A thickness as a function of distance from the ASG walls for both the Cleft and Vance segments. About half of the total percentage of thickening occurs abruptly within ~0.5 km of the ASG. Layer 2A then thickens progressively, reaching its full thickness (~90% and ~60% increase with respect to the on-axis thickness for the Cleft and Vance segments, respectively) at 3–4 km down the ridge flanks (Figure 13c).

[40] The two profiles that cross the OSC between the Cleft and Vance segments (lines 72 and 85, Figures 1 and 7) show thicker layer 2A at the axis of the Vance segment than at the Cleft segment, in agreement with previous results on layer 2A thickness derived from seismic refraction data [McDonald et al., 1994]. These observations are also in

agreement with results from a magnetic profile coincident with line 85 which show thicker magnetization layer beneath the Vance segment at the OSC [Tivey, 1994], supporting the idea that layer 2A is the primary magnetic source layer in ocean crust.

[41] The large number of profiles and good coverage of our data set allows us to map the variation in layer 2A thickness both along and across axis at a segment scale. We have interpolated the depth-converted layer 2A thickness measurements along all of our profiles onto an extrusive layer thickness map (Figure 14). The map shows that thin layer 2A (<350 m) is consistently limited to the ASG along both the Cleft and Vance segments, despite the large differences in ASG geometry between both segments. This observation is consistent with recent near-bottom magnetic measurements at the southern Cleft. A contrasting magnetization signature across the walls of the ASG suggests significant differences in the thickness of the magnetic source layer inside and outside of the ASG (Stakes et al., submitted manuscript, 2005).

[42] Along the Vance segment, the thinnest layer 2A (<300 m) correlates very well with the location of the AVRs. The band of thin layer 2A follows the eastern AVR along the northern half of the segment, and then bends westward near 45°17′N to follow the central AVR along the southern half of the segment (Figure 14). Outside of the ASG there is not a clear correlation between topography and areas of relatively thinner or thicker layer 2A (Figure 14b). The patches of locally thick layer 2A may correspond to structural features were lavas pond and accumulate, and/or to local, point source volcanism either on or off axis.

[43] The rapid off-axis thickening of layer 2A at fast and intermediate spreading ridges that display an axial-high morphology has been well documented [Harding et al., 1993; Kent et al., 1994; Carbotte et al., 1997, 1998; Blacic et al., 2004]. In general, layer 2A is thin at the ridge axis (~150–300 m), and thickens rapidly to ~350–600 m within just a few kilometers of the axis. Although off-axis volcanism has been documented [e.g., Perfit et al., 1994; Sims et al., 2003] and it may well be responsible for some of layer 2A thickening, the most compelling hypothesis is that topographic slopes driving channelized lava flows away from the injection zone at the ASCT largely control thickening of layer 2A at the EPR [e.g., Harding et al., 1993; Christeson et al., 1994; Hooft et al., 1996; Kurras et al., 2000; Fornari et al., 2004; Soule et al., 2005]. Stochastic models show that infrequent but voluminous eruptions that spill out of the ASCT can account for the layer 2A thickness observations [Hooft et al., 1996]. This model has been recently supported by observations at the GSC, where thickening of layer 2A by 150% is observed in the axial high domain of the ridge, in contrast to <40% of thickening

Figure 13. (a) Bathymetry and interpreted (top) base of layer 2A and (bottom) layer 2A thickness along line 74 across Cleft segment. The gray band marks the ASG. (b) Same as Figure 13a for line 69 across the Vance segment. Note that most of the thickening of layer 2A occurs rapidly at the walls of the ASG. Vertical scales in Figures 13a and 13b are two-way travel time in seconds. (c) Increase in off-axis layer 2A thickness (with respect to the average on-axis thickness) versus distance to the ASG for the Cleft (solid line with squares) and Vance (dashed line with circles) segments. Layer 2A thickness measurements along the across-axis profiles were binned every 0.5 km and then averaged for each segment. Gray areas bound the standard deviation from the mean (dark for Cleft, light for Vance). Note that within 0.5 km from the ASG, layer 2A has thickened by ~50% (Cleft) and ~30% (Vance) and that at both segments layer 2A continues thickening by roughly the same amounts up to 3–4 km from the ASG. No more significant thickening occurs beyond 4 km from the ASG.
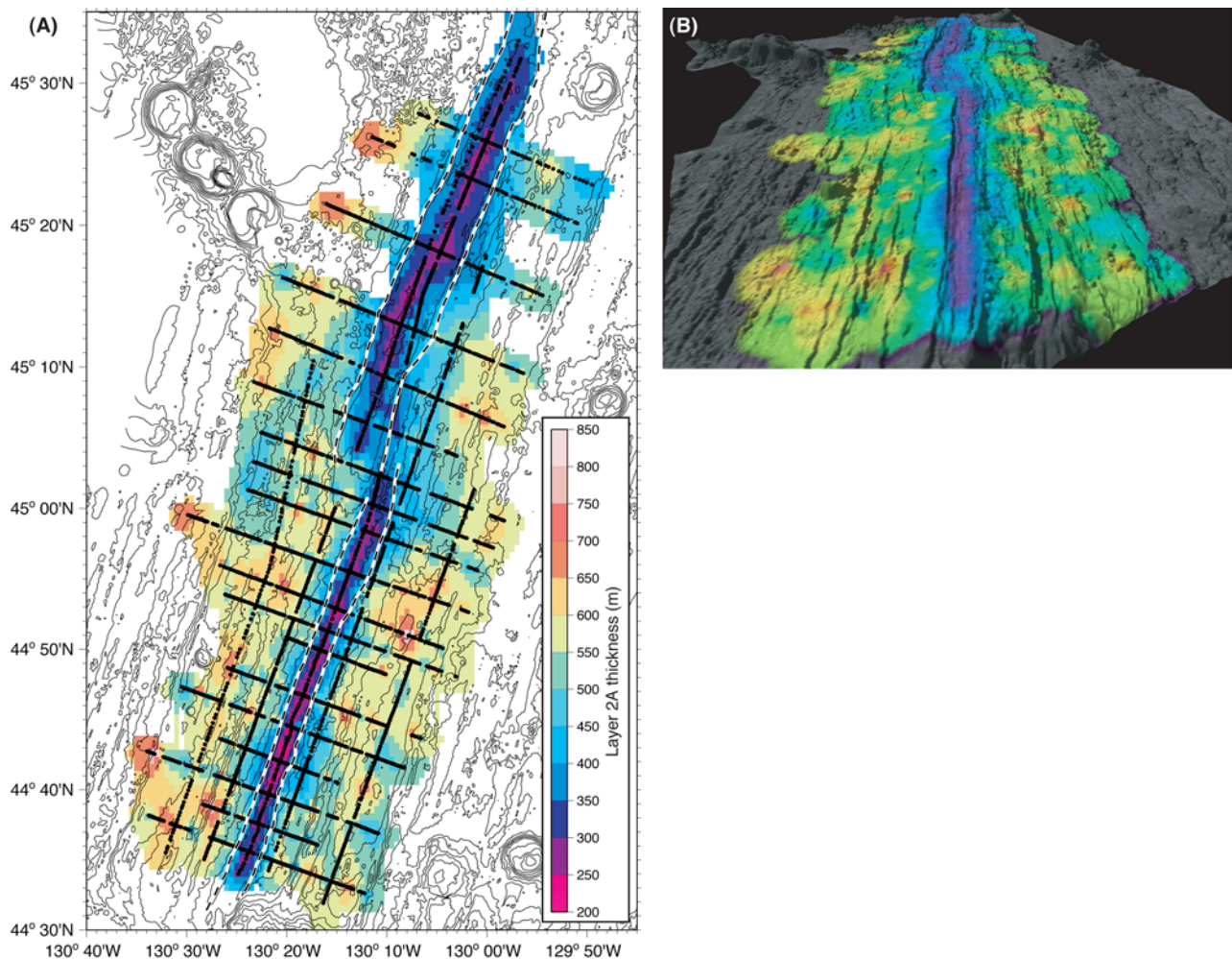
Figure 14. (a) Extrusive layer thickness map (color image). The layer 2A thickness measurements along the seismic profiles were interpolated onto a grid as a harmonic surface (no maxima or minima are possible except at the data points) using a continuous curvature algorithm [*Smith and Wessel*, 1990]. Contours are bathymetry every 100 m. Solid circles show the location of the layer 2A thickness picks used to make the map. Dashed lines show the location of the ASG walls, as interpreted from the bathymetry. (b) Three-dimensional perspective of the extrusive layer thickness map draped over the bathymetry (illumination from WNW, view from SSW). Note the excellent correlation between thin layer 2A (<350 m) and the ASG and the lack of correlation between areas of thick layer 2A and the flank abyssal hill topography.

where the morphology across the axis is transitional and nearly flat [*Blacic et al.*, 2004].

[44] The extrusive layer thickness map of Figure 14 has many common characteristics with similar maps from the southern EPR [*Kent et al.*, 1994; *Carbotte et al.*, 1997]. We suggest that processes of lava emplacement and layer 2A thickening along the southern JdFR are basically the same to those proposed for the fast spreading EPR. The main difference, the formation and role of the ASG in the evolution of layer 2A, will be discussed in section 6.

6. Discussion

6.1. Correlations Between Magma Lens, Layer 2A, Topography, and Spreading Rate: Comparison With the Galápagos Spreading Center

[45] Here we discuss the correlations we found between the AMC depth, layer 2A thickness, axial morphology,

spreading rate, and the geometry of the ASG, and compare them to similar observations along the western GSC [*Blacic et al.*, 2004]. The GSC is a hot spot-influenced ridge of intermediate spreading rate (53 mm/yr) along which magma supply variations related to the Galapagos hot spot largely affect ridge processes [*Detrick et al.*, 2002]. It is therefore an ideal natural laboratory where to study the influence of magma supply in crustal accretion processes independent of spreading rate [*Detrick et al.*, 2002]. Thus processes and models inferred from the GSC data [*Detrick et al.*, 2002; *Blacic et al.*, 2004] can be tested against our observations along the JdFR by comparing data from both ridges.

6.1.1. Magma Lens Depth, Axial Morphology, and Spreading Rate

[46] The AMC depth along the southern JdFR is consistent with the spreading rate dependence observed at other mid-ocean ridges [*Purdy et al.*, 1992]. The AMC is deeper than at faster spreading segments like the northern EPR at
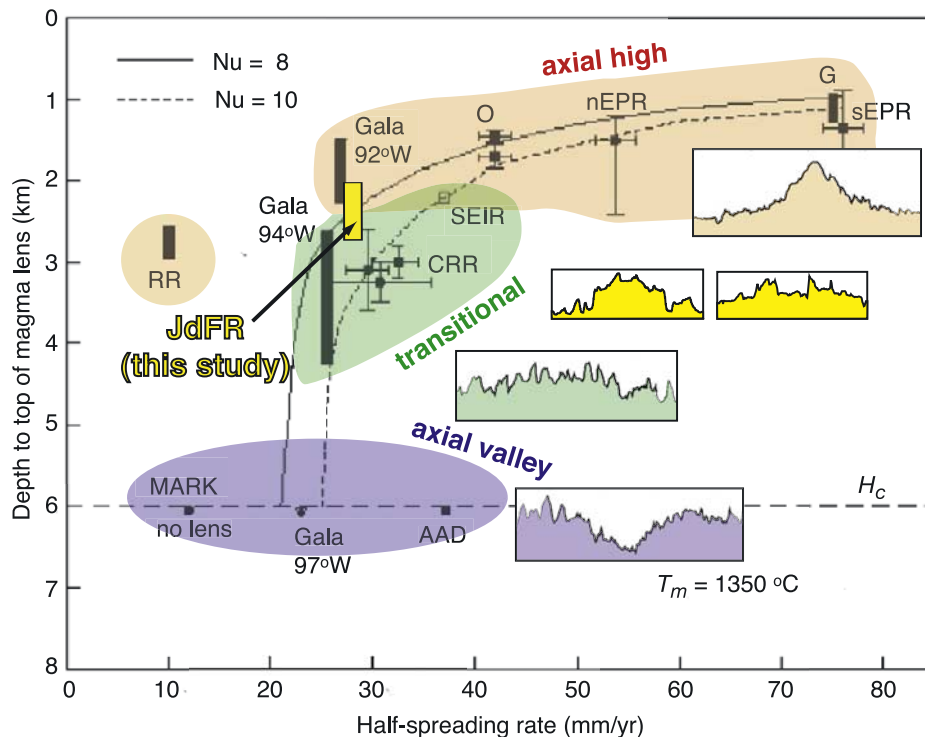
Figure 15. Observed and predicted AMC depth as a function of spreading rate (modified from *Chen and Lin* [2004] with permission from Elsevier). Solid and dashed lines show numerical results from *Chen and Lin* [2004] for a reference potential mantle temperature $T_m = 1350°C$, crustal thickness $H_c = 6$ km, and two values of the Nusselt number Nu (the ratio of convective to conductive heat transfer in a hydrothermal convection system). The yellow rectangle shows results from this study of the JdFR. Data from other spreading centers are GSC (Gala 92°W, 94°W), Reykjanes Ridge (RR), Costa Rica Rift (CRR), Southeast Indian Ridge (SEIR), EPR north of Orozco transform (O), EPR south of Garrett transform (G), northern EPR (nEPR), and southern EPR (sEPR). Locations where no magma lens has been found are plotted at a depth of 6 km: MAR south of Kane transform (MARK), GSC near 97°W, and the Australia-Antarctica Discordance (AAD). For more details, see Figure 3 of *Chen and Lin* [2004]. Insets show characteristic axial morphologies from the Galápagos Spreading Center at 92°W (axial high, orange), at 94°W (transitional, green), and at 97°W (axial valley, blue), and southern JdFR (rifted axial highs of Cleft and Vance segments, yellow). Shading areas bound data points from ridges with axial high (orange), transitional (green), and axial valley morphologies (blue).

16°N (85 mm/yr, AMC depth of 1.5–1.75 km) [*Carbotte et al.*, 1998], the northern EPR at 9°–10°N (111 mm/yr, AMC depth of 1.6 km) [*Detrick et al.*, 1987], and the southern EPR at 14°–17°S (155 mm/yr, AMC depth of 0.9–1.3 km) [*Detrick et al.*, 1993; *Kent et al.*, 1994; *Mutter et al.*, 1995]. The AMC along the southern JdFR is at comparable depths to other intermediate spreading ridges like the Lau Spreading Center (90–40 mm/yr, AMC depth of 1.3–2.9 km) [*Jacobs et al.*, 2003], the Endeavour segment at the northern JdFR (1.9–4.0 km) (E. van Ark et al., Seismic structure of the Endeavour segment, Juan de Fuca Ridge: Correlations with seismicity, faulting, and hydrothermal activity, manuscript in preparation, 2005), and the SEIR at 101°E (75 mm/yr, AMC depth of 1.9–2.3 km) [*Baran et al.*, 2005].

[47] Numerical models [*Phipps Morgan and Chen*, 1993b; *Chen and Lin*, 2004] show that at intermediate spreading rates the predicted AMC depth increases rapidly with decreasing spreading rate (i.e., magma supply) (Figure 15). This "threshold effect" indicates that small perturbations in magma supply could cause significant thermal reequilibration of the crustal magma system [*Chen and Lin*, 2004]. Recent observations from the western GSC [*Blacic et al.*, 2004] are consistent with these models. The AMC along the most hot spot-influenced part of the GSC is relatively shallow (1.0–2.5 km) and deeper (2.5–4.5 km) away from the hot spot [*Blacic et al.*, 2004]. One of the most striking observations at the GSC is the rapid deepening of the AMC as the morphology evolves from an axial high to a transitional style [*Blacic et al.*, 2004] despite the small change in magma supply in that area [*Canales et al.*, 2002], confirming the "threshold effect" predicted by numerical models [*Phipps Morgan and Chen*, 1993b]. The range of depths (2.0–2.7 km) we find in our study area corresponds to the depths of the AMC at the GSC where the threshold effect is observed (Figure 15).

[48] Axial topography is controlled by the strength of the axial lithosphere, which itself depends on the thermal structure [*Phipps Morgan and Chen*, 1993b]. The axial thermal structure reflects the balance of heat input to the
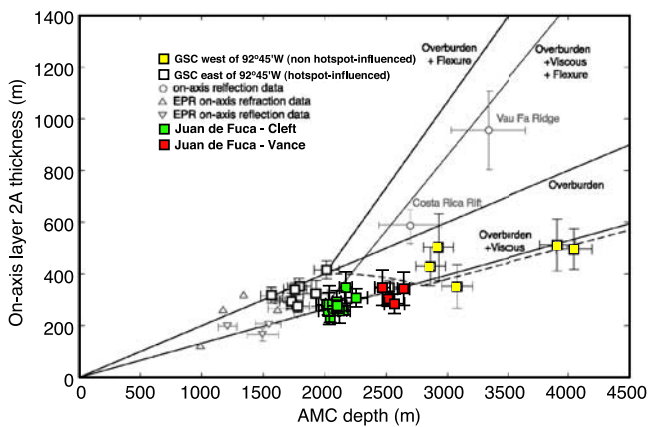
Figure 16. Correlation between depth to the magma lens and on-axis layer 2A thickness (modified from *Buck et al.* [1997] and *Blacic et al.* [2004]). Solid lines represent results of model calculations of *Buck et al.* [1997] for overburden alone and overburden plus other factors: dynamic pressure gradient (viscous) and increase in magma pressure due to regionally compensated topography (see *Buck et al.* [1997] for more details). Dashed line shows calculations by *Blacic et al.* [2004] including an increase in magma density at AMC depths of 2000–2800 m. Green and red squares represent data from this study for the Cleft and Vance segments, respectively. Open and yellow squares show data from the western GSC within and away from the hot spot-influenced area of the ridge, respectively. Data from other ridges are shown as triangles (EPR) and circles (Valu Fa Ridge and Costa Rica Rift).

crust by magma injection and heat removal by hydrothermal circulation. Thus changes in any of these two variables will ultimately affect the axial morphology; this effect being most pronounced at intermediate spreading rates [*Phipps Morgan and Chen*, 1993b; *Chen and Lin*, 2004]. Our observations from the southern JdFR shown in Figure 15 indicate that the axial morphology of the Cleft and Vance segment could change substantially if the axial thermal structure is perturbed. Such morphological changes can thus have an impact on how layer 2A is constructed. In section 6.3 we will explore in more detail this scenario and provide some constraints on the nature and magnitude of the perturbations to the axial thermal structure that could lead to the observed pattern of layer 2A thickness variations.

6.1.2. Magma Lens Depth and On-Axis Layer 2A Thickness

[49] *Buck et al.* [1997] postulated a simple model in which the balance between the pressure in the magma lens and the pressure needed to erupt magma on the surface through vertical dike injection from the magma lens leads to a positive correlation between the thickness of the extrusive layer at the axis and the depth to the magma lens. Observations at mid-ocean ridges of different spreading rates agree with this model (Figure 16), and our results also corroborate *Buck et al.*'s [1997] predictions: thicker on-axis layer 2A at Vance correlates with a deeper AMC. Thus the thicker on-axis layer 2A at Vance is a consequence of the pressure balance described above, and not a consequence of excess magmatism (e.g., due to the proximity of a seamount

chain to the west of this segment, Figure 1), which is mainly accommodated by changes in the thickness of the lower crust, not in the upper crust [e.g., *Tolstoy et al.*, 1993].

[50] The slope of the correlation depends on whether other factors affecting either the AMC pressure (e.g., regional rather than isostatic compensation) or the pressure within the dike (e.g., viscous pressure loss during magma flow), are taken into account [*Buck et al.*, 1997]. Data from the hot spot-influenced region of the GSC are consistent with the simplest case (overburden), while away from the influence of the hot spot the correlation requires either significant viscous pressure loss or a denser magma [*Blacic et al.*, 2004] (Figure 16).

[51] The positive correlation between AMC depth and on-axis layer 2A thickness at the southern JdFR follows the same trend observed in the western GSC away from the hot spot (Figure 16). For the GSC data away from the hot spot, *Blacic et al.* [2004] argued that the smaller slope of the correlation between AMC depth and on-axis layer 2A thickness could be explained by a higher magma density due to lower vesicularity and lower volatile content, without invoking viscous pressure loss. At the southern JdF, lava samples are Fe-rich ferrobasalts (i.e., denser) with a composition typical of normal mid-ocean ridge basalts (NMORB) [*Smith et al.*, 1994], and a volatile content comparable to the GSC NMORB samples west of the hot spot-affected section of the ridge [*Dixon et al.*, 1988; *Cushman et al.*, 2004]. Therefore we conclude that AMC depth and on-axis layer 2A thickness from the Cleft and Vance segments follow the same linear correlation as data from the western GSC (away from the hot spot) because of similar magma density due to similar volatile content and/or Fe enrichment, and do not require viscous pressure loss.

6.1.3. Layer 2A Thickening and Geometry of the Axial Summit Graben

[52] *Hooft et al.* [1996] suggest that the amount of off-axis thickening in layer 2A will depend, among other factors, on the length of the lava flows. Assuming that lava flows cannot overflow a well-developed axial graben, then wider axial grabens should allow flows to extend farther off axis, resulting in a positive correlation between axial graben width and amount of layer 2A thickening. Such correlation was not confirmed at the GSC, where *Blacic et al.* [2004] found that off-axis thickening of layer 2A was close to 0% where the axial graben was wider than 2 km. They suggested that other factors such as the slope of the ridge flank or the effusion rate might be more important than axial graben dimensions in controlling off-axis thickening of layer 2A. However, the GSC data also suggest that the axial graben is an effective barrier to off-axis lava flows, and as soon as ridge develops an axial graben that is wide enough (>2 km, Figure 17a), and/or deep enough (>100 m, Figure 17b), then the off-axis thickening of layer 2A is interrupted.

[53] If this hypothesis is correct, then wider and deeper axial grabens than that found at the GSC should not have significantly thicker off-axis layer 2A. However, our data from the JdFR contradicts this idea. The ASG along the Cleft segment is as wide and as deep as the axial graben along the GSC west of 94°W (Figures 17a and 7b), but layer 2A thickening outside of the ASG at Cleft is as large as the hot spot-influenced section of the GSC where the axial
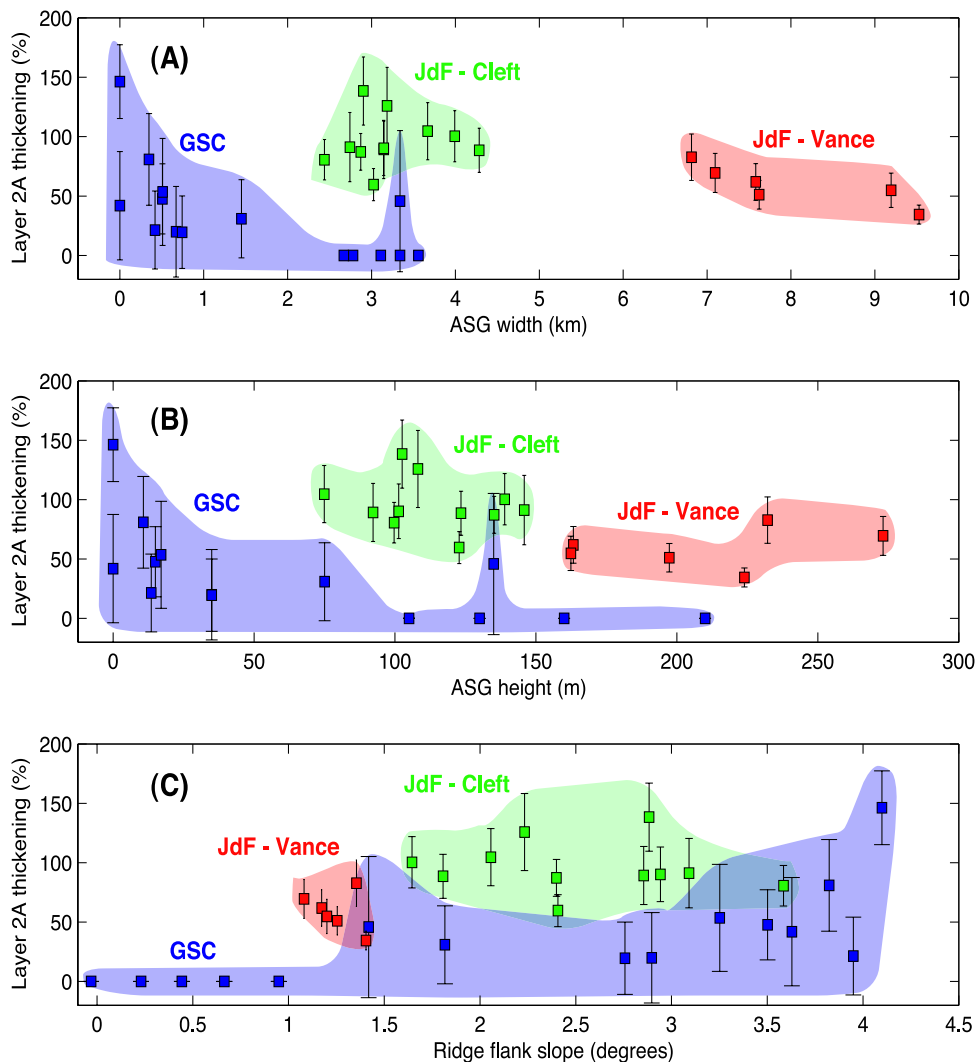
Figure 17. Correlations between the percentage of off-axis layer 2A thickening and (a) the width and (b) height of the ASG bounding walls and (c) the average ridge flank slope. Blue squares represent data from the GSC [*Blacic et al.*, 2004], and green and red squares represent results from this study (Cleft and Vance segments, respectively). The ASG width was measured as the distance between the summit of the bounding walls, and the ASG height is measured as the difference in depth between the summit of the bounding walls and the deepest part of the ASG floor. The ridge flank slope was measured from a linear fit of the topography across the ridge flank outside of the ASG in a 10-km-long window, averaging both the east and west flanks.

graben is very small or absent. The same is true for the Vance segment, where the ASG is much wider (∼7−9 km) and deeper (∼150−275 m) but off-axis layer 2A is ∼60% thicker than on axis.

[54] We explored the idea that the amount of off-axis thickening in layer 2A might be directly related to the slope of the ridge flanks. Data from both the GSC and the southern JdFR show that layer 2A thickening occurs wherever the ridge flanks have a slope larger then 1° (Figure 17c). For gentler slopes (i.e., nearly flat topography), the thickening of 2A is near zero at the GSC. Although we do not have observations at the southern JdFR where the flanks slopes are less than 1°, all of the observations shown in Figure 17 suggest that either the geometry of the ASG varies through time, allowing layer 2A to thicken off axis by downslope lava flows when the ASG is narrow

and shallow, or that other processes such as off-axis volcanism contribute significantly to the thickening of layer 2A. These two alternatives are discussed in more detail in the following section.

6.2. Evidence for Temporal Evolution of Ridge Crest Relief

[55] *Kappel and Ryan* [1986] argued that the ASG walls along the JdFR are not steady state features. The segment-scale pattern of layer 2A thickening (Figure 14) obtained from our seismic data is new evidence confirming that the ASG along the southern JdFR is not a permanent morphological feature. If the ASG were a steady state feature, and if the thickening of layer 2A occurs in a similar way as at the EPR, then there would have to be voluminous lava eruptions large enough to fill up the ASG and overflow off
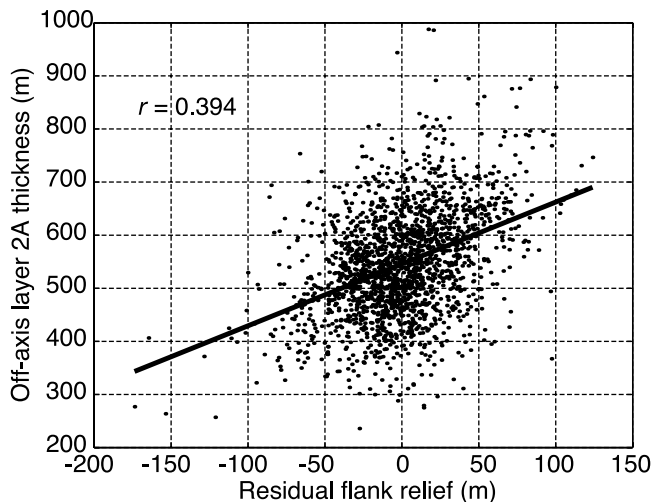
Figure 18. Scatterplot of off-axis layer 2A thickness measurements versus residual flank relief. Layer 2A thickness measurements along the across-axis profiles were averaged in 125-m-wide bins. The residual relief was measured as the difference between the flank bathymetry along the across-axis lines outside the ASG and a fourth-order polynomial fit to the flank topography (east and west flanks were fit separately). Solid line is the least squares linear fit to the data points. Although there seems to be a positive correlation with larger flank relief having thicker layer 2A, the linear correlation coefficient r between both observables is too low to consider this correlation significant.

axis in order to explain the thicker layer 2A off axis. Given the dimensions of the ASG, the volume of these flows would have to be of the order of $\sim 240 \times 10^6 \, \text{m}^3$ and $\sim 1200 \times 10^6 \, \text{m}^3$ per kilometer of ridge length for the Cleft and Vance segments, respectively. These volumes are ~ 20 to ~ 140 times larger than previous estimates in this area from seafloor observations [*Perfit and Chadwick*, 1998], and argue against lava flooding of the ASG with its present dimensions as the dominant process for layer 2A thickening.

[56] We explored two other ways of thickening layer 2A with a steady state ASG. The first hypothesis assumes that the base of layer 2A, rather than being a lithological boundary, represents an alteration front produced by the increase in porosity as cracks and fissures develop and penetrate the upper crust as the crust spreads [e.g., *McClain et al.*, 1985]. In this scenario the ASG could be a steady state tectonic feature and the layer 2A thickness map of Figure 14 would represent the evolution of upper crustal porosity. However, there are convincing observations that place the base of seismic layer 2A near the extrusive/dikes boundary in exposed sections of oceanic crust [*Christeson and McIntosh*, 2003], arguing against this model.

[57] The second alternative involves off-axis volcanism. Off-axis eruptions as far as a few km from the ASCT have been reported before at the EPR [e.g., *Goldstein et al.*, 1994; *Perfit et al.*, 1994; *Sims et al.*, 2003], and a physical mechanism to explain them has been recently proposed [*Sohn and Sims*, 2005]. However, if off-axis eruptions outside of the ASG were a process common enough to thicken layer 2A by 60–90% in such as consistent manner

along both segments as Figure 14 indicates, evidence of them should had been found more extensively. Also, off-axis volcanism appears to be related to faulting and abyssal hills [*Macdonald et al.*, 1996]. Thus one would expect some correlation between abyssal hills and thicker 2A; correlation that we do not find (Figure 14).

[58] Recent submersible observations at the Cleft segment have documented the presence of lava flows that emanate from faults and fissures within the ASG, capping its walls [*Perfit et al.*, 2003; Stakes et al., submitted manuscript, 2005]. The evolved nature of these lavas suggests that they erupted from the cooler, distal edges of the AMC. Thus at least part of the thickening of layer 2A must take place by eruptions along the ASG walls. The question, however, is how significant is this process for the construction of layer 2A. In the steady state ASG scenario, eruptions from the cooler, distal edges of the AMC along the Cleft ASG shoulders would have to produce nearly the same volume of extrusive lavas as eruptions from the axis above the hotter center of the AMC. This hypothesis also predicts that within the extrusive section of mature intermediate spreading rate crust, the lower lavas should be predominantly more primitive (erupted on axis) than the upper lavas (erupted off axis from the edges of the AMC). This prediction is not supported by data from the Deep Sea Drilling Project/Ocean Drilling Program Hole 504B (drilled in ocean crust formed at the intermediate spreading rate Costa Rica Rift), which show mostly primitive lavas with MgO content ranging from 7 to 9.5 wt % without significant differences between the upper and lower lavas within the first 1000 m of the hole [*Pedersen and Furnes*, 2001].

[59] The last piece of evidence that links the ASG to a transient feature related to magmatic processes comes from the correlation between the presence of the ASG and the presence of the AMC. Along the full length of the JdFR, *Carbotte et al.* [2005] found a close spatial correlation between where a crustal AMC is imaged and where the axial graben is well defined. These authors argue that if the ASG where a steady state tectonic feature, it should be well developed where the AMC is absent, contrary to the observations. Therefore we conclude that the ASG is a transient feature, most likely periodic (as suggested by the regular spacing of the abyssal hills along the ridge flanks), and that most of the thickening of layer 2A occurs during periods when the ASG is absent or small enough that reasonably large eruptions can overflow it.

6.3. Nature of the Episodicity of Ridge Crest Relief

[60] *Kappel and Ryan* [1986] suggested that the abyssal hills and shoulders of the ASG were constructed episodically during periods of significantly enhanced volcanism, and then were rifted apart during a less magmatic period. While most of our observations are consistent with this model of episodic volcanism, one would expect some correlation between the presence of abyssal hills and thicker layer 2A off axis. Off-axis layer 2A thickness correlates only very weakly with flank relief (Figure 18), therefore questioning the idea that the abyssal hills and ASG walls formed during episodes of increased volcanism. At the Endeavour segment *Barclay and Wilcock* [2004] argue that ridge-parallel bands of low upper crustal seismic velocity correlate with abyssal hills, suggesting 100–200 m thicker
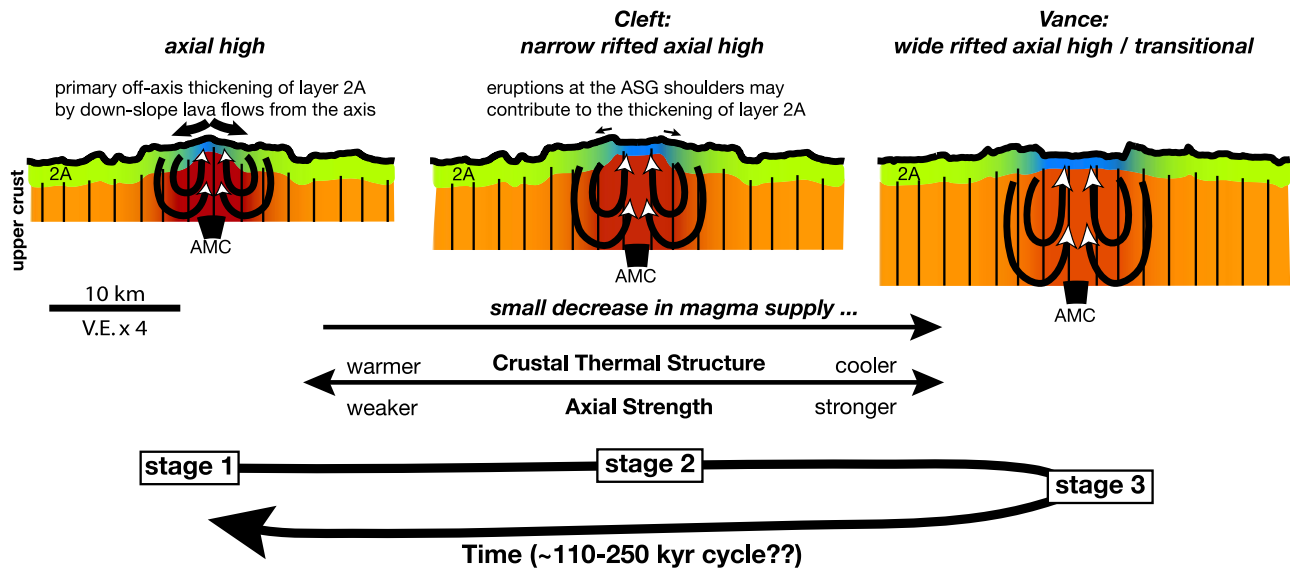
Figure 19. Conceptual model of the evolution of the upper crustal structure (layer 2A thickness and AMC depth) and axial morphology of an intermediate spreading rate ridge due to small fluctuations in magma supply (see text for details).

layer 2A beneath topographic highs. Our analysis does not support a similar correlation at the Cleft and Vance segments.

[61] We have considered the hypothesis that the ASG forms and evolves due to episodic, small perturbations in magma supply that result in large changes in axial yield strength and thermal structure [*Phipps Morgan and Chen*, 1993b] without significantly increased magmatism. Studies along the GSC show clearly the strong dependence of axial morphology and AMC depth with magma supply; axial morphology and AMC depth vary quite sharply along the GSC together with minimal changes in magma supply [*Canales et al.*, 1997, 2002; *Detrick et al.*, 2002; *Sinton et al.*, 2003; *Blacic et al.*, 2004; *Chen and Lin*, 2004]. At the southern JdFR, the AMC depth and spreading rate are such that axial morphology could oscillate between a well-developed EPR-like axial high like that observed at the GSC near 92°W, and the transitional style of the GSC near 94°W (Figure 15).

[62] In this hypothesis, subtle changes in magma supply (which can be small enough so the total crustal production and the volume of volcanism are not significantly altered) can produce significant changes in AMC depth. This would allow temporal variations in the thermal structure of the crust as the efficiency of cooling by hydrothermal circulation increases as the AMC deepens [*Phipps Morgan and Chen*, 1993b], driving the spreading segment back and forth through a series of axial morphologies ranging from an EPR-like axial high, to a rifted axial high with a narrow ASG (e.g., Cleft morphology), and eventually to a stage where the ASG is wide and deep (e.g., Vance morphology) (Figure 19). In this scenario, the different AMC depths found at Cleft and Vance segments would reflect their different axial thermal stages within this cyclic model. The off-axis thickening of layer 2A thus would occur when the segment is most inflated (so lavas can effectively be transported down the ridge flanks) and the ASG is absent or small. This would explain why the thin layer 2A is always confined to within the ASG walls (Figure 14).

[63] On the basis of topography and gravity data, *Hooft and Detrick* [1995] suggest that the large difference in axial morphology between the Cleft segment and the northern Gorda Ridge (south of the JdFR, offset from the Cleft segment by the ~400-km-long Blanco Fracture Zone) arises from a 10°–15°C difference in mantle temperature that results in no more than 300 m of difference in crustal thickness between both ridge segments. Both segments have similar spreading rate, but the northern Gorda Ridge is characterized by a ~14-km-wide, ~1000-m-deep axial valley. Therefore we can infer that the magma supply variations postulated in our model should produce no more than 100–200 m variations in total crustal thickness, since the morphological difference between an EPR-like axial high, the Cleft, and the Vance segments are less pronounced than those between the Cleft and the northern Gorda segments. Such small changes in total crustal production are at the limit of resolution of seismic reflection methods, and therefore consistent with the nearly constant two-way travel time to Moho observed across the flanks of the Cleft segment within 20 km from the ridge axis [*Nedimović et al.*, 2005].

[64] The variations in axial thermal structure may arise from small temporal variations in mantle melt productivity (either thermal or compositional in origin), but they also could reflect temporal fluctuations on the efficiency of melt delivery from the mantle to the crust. Alternatively, the evolutionary stages described above could be achieved by small changes in the efficiency of heat extraction by hydrothermal circulation, rather than by changes in magma supply. Changes in the efficiency of hydrothermal circulation could be produced by opening of new water pathways by faulting, and/or by sealing of existing pathways by mineral deposition. The mechanisms of hydrothermal circulation are still not well understood, and it is unclear to us why and how these changes could operate synchronously along a >60-km-long segment.

[65] It is important to note that although our model has similarities with *Kappel and Ryan*'s [1986] model, it also

has important differences. In this "thermal" model the ridges forming the ASG shoulders are not necessarily formed by enhanced or robust magmatism; they form by flexural uplift of the ridge axis (as described in the accretional curvature model of *Buck* [2001]) after a decrease in axial yield strength [*Phipps Morgan and Chen*, 1993b], and then rifted apart as the axial yield strength increases.

[66] We can estimate the timescale of this evolution from the spacing of the abyssal hills along the ridge flanks. The spacing between the split volcanic ridges ranges between ∼3 and ∼7 km (Figures 1 and 2), which corresponds to timescales in the order of ∼110 to ∼250 kyr. It is likely that the subtle magma supply variations we propose are a common process at all spreading rates along the global mid-ocean ridge system. However, their effects are only noticeable at these critical intermediate spreading rates where axial thermal structure is most sensitive to changes in magma supply [*Phipps Morgan and Chen*, 1993b].

[67] While this "thermal" model explains all of our observations at the southern JdFR, there are some aspects that do not quite fit with observations along other segments of the JdFR. For example, none of the segments along the JdFR have an EPR-like axial high morphology that could be indicative of the stage 1 represented in Figure 19 (although this type of morphology is present along other intermediate spreading rate ridges not affected by hot spots, like segments S1, S2, and P1 along the SEIR [*Cochran et al.*, 1997]). Also, the average AMC depth along the Northern Symmetrical segment at the JdFR (46°30′N–47°45′N), is comparable to the Vance segment (hence having similar axial thermal structure) but the ASG is much narrower [*Carbotte et al.*, 2005]. On the basis of correlations between ASG geometry and the AMC along the JdFR, *Carbotte et al.* [2005] propose a model in which the ASG is an evolving feature controlled by magmatic processes and feedbacks between magmatic events and the rheology of the upper crust. In their model the ridge crest relief is linked to faulting associated with dike injection, similar to that documented within rift zones in Iceland and Hawaii [*Rubin and Pollard*, 1988; *Rubin*, 1992]. In this case the ASG evolves from an AVR to a wide ASG, not through a reduction in magma supply and deepening of the AMC, but rather through graben formation and ongoing faulting and subsidence associated with magma movements and successive diking events.

[68] Both models are not necessarily mutually exclusive; there is no reason why temporal variations in axial morphology cannot be accompanied by diking-induced graben formation. The small changes in magma supply that result in the observed differences in AMC depth could also influence the dike-induced faulting mechanism of *Carbotte et al.* [2005]; shallower magma bodies must result in shorter dike heights and perhaps more frequent dike intrusions, thus having an impact on ambient stresses. In both cases the off-axis thickening of layer 2A occurs when the ASG is narrow and occasional eruptions can flood the graben and overflow the flanks. The process of layer 2A thickening is then as proposed by *Hooft et al.* [1996], a view supported by the magnetization pattern observed in ∼0.8–1.2 Ma section of upper crust exposed along the northern scarp of the Blanco fracture zone [*Tivey et al.*, 1998]. As Figure 13c indicates, layer 2A thickening takes place within 3–4 km from the

ASG, which is also consistent with the maximum distance (∼3 km) that lavas can flow down the ridge flanks in this area as inferred from magnetic data [*Tivey et al.*, 1998]. As the ASG widens, fewer eruptions would be able to overflow it, eventually interrupting the off-axis thickening of layer 2A and resulting in the pattern of relatively thin layer 2A confined within the ASG shown in Figure 14.

[69] The Vance segment could be now evolving from stage 3 back to stage 1 (Figure 19), or it could be in the early stages of AVR development in Carbotte et al.'s model, as suggested by the presence of the two AVRs along the segment. Also, the thickening of layer 2A due to the presence of these small-relief AVRs is already noticeable; layer 2A in thinnest along the summit of the AVRs and thickens moderately away from them within the Vance ASG (Figure 14).

[70] Furthermore, both models are consistent with recent submersible observations and petrological analyses conducted along the Cleft segment [*Perfit et al.*, 2003; Stakes et al., submitted manuscript, 2005]. When the axial high or the AVR are developed, most of the lavas transported off axis and forming the bulk of layer 2A thickening would be mostly primitive. After the ASG develops and is wide enough, the bounding faults could penetrate down to the AMC depth and act as pathways for eruptions capping the ASG walls. As the ASG continues to widen, the bounding faults start to reach the cooler edges of the AMC, allowing the off-axis eruption of more evolved lavas, as proposed by *Perfit et al.* [2003] and Stakes et al. (submitted manuscript, 2005), that would cover the more primitive lavas erupted during the axial high or AVR stage. These eruptions would also contribute to the sharp contrast in layer 2A thickness observed along the ASG walls (Figure 14). However, they probably contribute only a small fraction to the off-axis thickening of layer 2A. Where the AMC is deeper, like at Vance, the faults forming the ASG should interact for longer time with the AMC. Thus if eruptions emanating from these faults were significantly voluminous, they should result in noticeable thicker off-axis layer 2A at Vance when compare to Cleft, a prediction not supported by our observations (Figure 12b).

[71] An interesting question is that if the ASG walls are such effective barriers for lava flows, why on-axis layer 2A appears not to be significantly thickened once the ASG is wide and deep if the entire lava emplacement occurs within the ASG? In our study area, average layer 2A off-axis thickness (Figure 12b) is similar to that of the EPR (400–600 m [e.g., *Harding et al.*, 1993]), but average on-axis thickness (Figure 12b) is larger than at the EPR (200 m [e.g., *Harding et al.*, 1993]). This implies that on-axis layer 2A has in fact thickened by ∼50–100 m at Cleft, and by ∼100–150 m at Vance. Numerical models similar to that of *Hooft et al.* [1996] that incorporate the presence and effects of an ASG with variable dimensions over time will be required to better understand the observed pattern of layer 2A thickness.

7. Conclusions

[72] We have imaged the upper crustal structure of 0–620 ka crust along the southern JdFR using modern multichannel seismic reflection data. From our interpreta-

tion of the time-migrated seismic images we make the following conclusions:

[73] 1. Along most of the Cleft and Vance segments at the southern JdFR the ridge axis is underlain by an AMC that systematically deepens from 2.0 km at the RIDGE Cleft Observatory site near the southern end of the Cleft segment, to 2.7 km near the northern end of the Vance segment. A high-amplitude AMC is present beneath all of the known high-temperature vent fields, and beneath the site of the 1980s eruptive event at the northern Cleft segment.

[74] 2. The extrusive layer (seismic layer 2A) is 250–350 m thick within the ASG that marks the spreading axis in this area and thickens off axis by ~90% and ~60% at the Cleft and Vance segments, respectively. Half of the thickening occurs sharply at the walls of the ASG, despite the large differences in size between the Cleft and Vance segment's ASG. Layer 2A reaches its full off-axis thickness ~3–4 km down the ridge flanks, constraining the distance that lavas can flow off axis at this spreading ridge. The segment-scale pattern of layer 2A thickening is similar to that observed at the fast spreading EPR, and is probably a consequence of lava transport from the injection zone to the ridge flanks by the topographic slopes of the axial high.

[75] 3. Off-axis layer 2A thickness is similar at the Cleft and Vance segments, despite the large difference in ASG geometry. The correlations we find between off-axis layer 2A thickness, axial graben geometry, and ridge flank slope, when compared to similar observations along the Galápagos Spreading Center, are inconsistent with the hypothesis of the ASG being a steady state feature, and indicate that ridge flank slope is an important factor controlling the amount of layer 2A thickening. Also, the weak correlation between off-axis layer 2A thickness and flank relief argues against the abyssal hills being volcanic constructional highs formed during periods of enhanced volcanism.

[76] 4. On-axis layer 2A thickness correlates positively with the depth to the AMC, corroborating previous models in which the pressure needed to erupt a vertical dike is balanced by the overburden pressure in the magma lens.

[77] 5. Patterns of layer 2A thickness indicate that the axial region experiences a phase when the ASG is absent or narrow and layer 2A accumulations occurs by downslope transport in a similar manner as observed at the EPR. During this phase relatively large eruptions can overflow the ASG, emplacing the lavas up to 3–4 km from the axis and contributing to the off-axis thickening of layer 2A. As the ASG widens and deepens, the ASG walls become effective barriers for lava flows, resulting in the striking spatial correlation between relatively thin layer 2A and the ASG.

[78] 6. The observed depth of the AMC falls at the "threshold" transition from an axial high with shallow AMC to a transitional morphology with deeper AMC predicted by numerical models, underlining the importance of magma supply control on ridge structure at these intermediate spreading rates. Thus the evolution of the ASG could be related to temporal changes in axial morphology due to subtle fluctuations in magma supply. The changes in magma supply can be small enough so that the total crustal thickness is not significantly affected, but have a significant impact on the axial thermal structure because of the inter-

mediate spreading rate. Therefore the ASG shoulders and abyssal hills are not formed by enhanced volcanism, as previously proposed, but rather by flexural uplift of the plate boundary when the axial yield strength is low, and then rifted apart as the lithosphere becomes colder and stronger.

[79] 7. The fluctuations in magma supply that result in such large changes in axial morphology at intermediate spreading rates are likely to occur at all spreading rates, but their effects are most noticeable at these critical intermediate spreading rates.

References

Applegate, T. B. (1990), Volcanic and structural morphology of the South flank of Axial Volcano, Juan de Fuca Ridge: Results from a Sea MARC I side scan sonar survey, *J. Geophys. Res.*, *95*(B8), 12,765–12,783.

Baker, E. T., W. Lavelle, R. A. Feely, G. J. Massoth, and C. L. Walker (1989), Episodic venting on the Juan de Fuca Ridge, *J. Geophys. Res.*, *94*, 9237–9250.

Baran, J. M., J. R. Cochran, S. M. Carbotte, and M. R. Nedimović (2005), Variations in upper crustal structure due to variable mantle temperature along the Southeast Indian Ridge, *Geochem. Geophys. Geosyst.*, *6*, Q11002, doi:10.1029/2005GC000943.

Barclay, A. H., and W. S. D. Wilcock (2004), Upper crustal seismic velocity structure and microearthquake depths at the Endeavour Segment, Juan de Fuca Ridge, *Geochem. Geophys. Geosyst.*, *5*, Q01004, doi:10.1029/2003GC000604.

Blacic, T. M., G. Ito, J. P. Canales, R. S. Detrick, and J. M. Sinton (2004), Constructing the crust along the Galapagos Spreading Center 91.3°–95.5°W: Correlation of seismic layer 2A with axial magma lens and topographic characteristics, *J. Geophys. Res.*, *109*, B10310, doi:10.1029/2004JB003066.

Buck, W. R. (2001), Accretional curvature of lithosphere at magmatic spreading centers and the flexural support of axial highs, *J. Geophys. Res.*, *106*, 3953–3960.

Buck, W. R., S. M. Carbotte, and C. Mutter (1997), Controls on extrusion at mid-ocean ridges, *Geology*, *25*, 935–938.

Canales, J. P., J. J. Dañobeitia, R. S. Detrick, E. E. E. Hooft, R. Bartolomé, and D. F. Naar (1997), Variations in axial morphology along the Galápagos spreading center and the influence of the Galápagos hotspot, *J. Geophys. Res.*, *102*, 27,341–27,354.

Canales, J. P., G. Ito, R. S. Detrick, and J. M. Sinton (2002), Crustal thickness along the western Galápagos Spreading Center and the compensation of the Galápagos hotspot swell, *Earth Planet. Sci. Lett.*, *203*(1), 311–327.

Canales, J. P., S. C. Singh, R. S. Detrick, S. M. Carbotte, G. M. Kent, J. B. Diebold, A. J. Harding, M. R. Nedimović, and J. Babcock (2004), Seismic structure of the axial magma chamber along the southern Juan de Fuca Ridge from full-waveform inversion and partial S-wave stacking, *Eos Trans. AGU*, *85*(47), Fall Meet. Suppl., Abstract B13A-0182.

Carbotte, S. M., J. C. Mutter, and L. Xu (1997), Contribution of volcanism and tectonism to axial and flank morphology of the southern East Pacific Rise, 17°10′–17°40′S, from a study of layer 2A geometry, *J. Geophys. Res.*, *102*, 10,165–10,184.

Carbotte, S. M., C. Mutter, J. C. Mutter, and G. Ponce-Correa (1998), Influence of magma supply and spreading rate on crustal magma bodies

and emplacement of the extrusive layer: Insights from the East Pacific Rise at lat 16°N, *Geology*, *26*, 455–458.

Carbotte, S. M., et al. (2002), A multi-channel seismic investigation of the ridge crest and ridge flank structure along the Juan de Fuca Ridge, *Eos Trans. AGU*, *87*(47), Fall Meet. Suppl., Abstract T72C-07.

Chadwell, C. D., J. A. Hildebrand, F. N. Spiess, J. L. Morton, W. R. Normark, and C. A. Reiss (1999), No spreading across the southern Juan de Fuca ridge axial Cleft during 1994–1996, *Geophys. Res. Lett.*, *26*(16), 2525–2528.

Chadwick, W. W., and R. W. Embley (1994), Lava flows from a mid-1980s submarine eruption on the Cleft segment, Juan de Fuca Ridge, *J. Geophys. Res.*, *99*, 4761–4776.

Chadwick, W. W., R. W. Embley, and C. G. Fox (1991), Evidence for volcanic eruptions on the southern Juan de Fuca Ridge between 1981 and 1987, *Nature*, *350*, 416–418.

Chadwick, W. W., et al. (2001a), The RIDGE Observatory at the Cleft segment: Investigation of linkages between geodetic, geophysical, geochemical, and water column processes, *RIDGE Events*, *11*(1), 18–24.

Chadwick, W. W., D. S. Scheirer, R. W. Embley, and H. P. Johnson (2001b), High-resolution bathymetric surveys using scanning sonars: Lava flow morphology, hydrothermal vents, and geologic structure at recent eruption sites on the Juan de Fuca Ridge, *J. Geophys. Res.*, *106*, 16,075–16,099.

Chen, Y. J., and J. Lin (2004), High sensitivity of ocean ridge thermal structure to changes in magma supply: The Galápagos Spreading Center, *Earth Planet. Sci. Lett.*, *221*, 263–273.

Christeson, G. L., and K. McIntosh (2003), Correlation of shallow seismic structure and observed geologic boundaries of fast-spreading crust exposed near Hess Deep, *Eos Trans. AGU*, *84*(46), Fall Meet. Suppl., Abstract T11B-04.

Christeson, G. L., G. M. Purdy, and G. J. Fryer (1994), Seismic constraints on shallow crustal emplacement processes at the fast spreading East Pacific Rise, *J. Geophys. Res.*, *99*, 17,957–17,973.

Cochran, J. R., J. Sempéré, and SEIR Scientific Team (1997), The Southeast Indian Ridge between 88°E and 118°E: Gravity anomalies and crustal accretion at intermediate spreading rates, *J. Geophys. Res.*, *102*, 15,463–15,488.

Cudrak, C. F., and R. M. Clowes (1993), Crustal structure of Endeavour Ridge Segment, Juan de Fuca Ridge, from a detailed seismic refraction survey, *J. Geophys. Res.*, *98*, 6329–6349.

Cushman, B., J. Sinton, G. Ito, and J. Eaby Dixon (2004), Glass compositions, plume-ridge interaction, and hydrous melting along the Galápagos Spreading Center, 90.5°W to 98°W, *Geochem. Geophys. Geosyst.*, *5*, Q08E17, doi:10.1029/2004GC000709.

Detrick, R. S., P. Buhl, E. E. Vera, J. C. Mutter, J. A. Orcutt, J. A. Madsen, and T. M. Brocher (1987), Multi-channel seismic imaging of a crustal magma chamber along the East Pacific Rise, *Nature*, *326*, 35–41.

Detrick, R. S., A. J. Harding, G. M. Kent, J. A. Orcutt, J. C. Mutter, and P. Buhl (1993), Seismic structure of the southern East Pacific Rise, *Science*, *259*, 499–503.

Detrick, R. S., J. A. Collins, R. A. Stephen, and S. A. Swift (1994), In situ evidence for the nature of the seismic layer 2/3 boundary in oceanic crust, *Nature*, *370*, 288–290.

Detrick, R. S., et al. (2002), Correlated geophysical, geochemical and volcanological manifestations of plume-ridge interaction along the Galapagos Spreading Center, *Geochem. Geophys. Geosyst.*, *3*(10), 8501, doi:10.1029/2002GC000350.

Dixon, J. E., E. M. Stolper, and J. R. Delaney (1988), Infrared spectroscopic measurements of CO_2 and H_2O in Juan de Fuca Ridge basaltic glasses, *Earth Planet. Sci. Lett.*, *90*, 87–104.

Dunn, R. A., D. R. Toomey, and S. C. Solomon (2000), Three-dimensional seismic structure and physical properties of the crust and shallow mantle beneath the East Pacific Rise at 9°30′N, *J. Geophys. Res.*, *105*, 23,537–23,555.

Embley, R. W., and W. W. Chadwick Jr. (1994), Volcanic and hydrothermal processes associated with a recent phase of seafloor spreading at the northern Cleft segment: Juan de Fuca Ridge, *J. Geophys. Res.*, *99*, 4741–4760.

Embley, R. W., J. Chadwick, W. William, M. R. Perfit, and E. T. Baker (1991), Geology of the northern Cleft segment, Juan de Fuca Ridge: Recent lava flows, sea-floor spreading, and the formation of megaplumes, *Geology*, *19*, 771–775.

Evans, R., S. C. Webb, M. Jegen, and K. Sananikone (1998), Hydrothermal circulation at the Cleft-Vance overlapping spreading center: Results of a magnetometric resistivity study, *J. Geophys. Res.*, *103*, 12,321–12,338.

Fornari, D. J., R. M. Haymon, M. R. Perfit, T. K. P. Gregg, and M. H. Edwards (1998), Axial summit trough of the East Pacific Rise 9°–10°N: Geological characteristics and evolution of the axial zone on fast spreading mid-ocean ridges, *J. Geophys. Res.*, *103*, 9827–9855.

Fornari, D. J., et al. (2004), Submarine lava flow emplacement at the East Pacific Rise 9°50′N: Implications for uppermost ocean crust stratigraphy and hydrothermal fluid circulation, in *The Thermal Structure of the Ocean Crust and the Dynamics of Hydrothermal Circulation, Geophys. Monogr. Ser.*, vol. 148, pp. 187–217, AGU, Washington, D. C.

Forsyth, D. W. (1993), Crustal thickness and the average depth and degree of melting in fractional melting models of passive flow beneath mid-ocean ridges, *J. Geophys. Res.*, *98*, 16,073–16,079.

Goldstein, S. J., M. R. Perfit, R. Batiza, D. J. Fornari, and M. T. Murrell (1994), Off-axis volcanism at the East Pacific Rise detected by uranium-series dating of basalts, *Nature*, *367*, 157–159.

Grevemeyer, I., and W. Weigel (1996), Seismic velocities of the uppermost igneous crust versus age, *Geophys. J. Int.*, *124*, 631–635.

Harding, A. J., G. M. Kent, and J. A. Orcutt (1993), A multichannel seismic investigation of upper crustal structure at 9°N on the East Pacific Rise: Implications for crustal accretion, *J. Geophys. Res.*, *98*, 13,925–13,944.

Herron, T. J. (1982), Lava flow layer-East Pacific Rise, *Geophys. Res. Lett.*, *9*(1), 17–20.

Herron, T. J., W. J. Ludwig, P. L. Stoffa, T. K. Kan, and P. Buhl (1978), Structure of the East Pacific Rise crest from multichannel seismic reflection data, *J. Geophys. Res.*, *83*, 798–804.

Hooft, E. E. E., and R. S. Detrick (1995), Relationship between axial morphology, crustal thickness, and mantle temperature along the Juan de Fuca and Gorda ridges, *J. Geophys. Res.*, *100*, 22,499–22,508.

Hooft, E. E. E., H. Schouten, and R. S. Detrick (1996), Constraining crustal emplacement processes from the variation in seismic layer 2A thickness at the East Pacific Rise, *Earth Planet. Sci. Lett.*, *142*, 289–309.

Houtz, R. E., and J. Ewing (1976), Upper crustal structure as a function of plate age, *J. Geophys. Res.*, *81*, 2490–2498.

Hussenoeder, S. A., R. S. Detrick, G. M. Kent, H. Schouten, and A. J. Harding (2002), Fine-scale seismic structure of young upper crust at 17°20′S on the fast spreading East Pacific Rise, *J. Geophys. Res.*, *107*(B8), 2158, doi:10.1029/2001JB001688.

Jacobs, A., A. J. Harding, G. M. Kent, and J. A. Collins (2003), Along-axis crustal structure of the Lau back-arc basin from multichannel seismic observations, *Eos Trans. AGU*, *84*(46), Fall Meet. Suppl., Abstract B12A-0728.

Kappel, E. S., and W. B. F. Ryan (1986), Volcanic episodicity and a non-steady state rift valley along the Northeast Pacific spreading centers: Evidence from Sea MARC I, *J. Geophys. Res.*, *91*, 13,925–13,940.

Kelemen, P. B., K. Koga, and N. Shimizu (1997), Geochemistry of gabbro sills in the crust-mantle transition zone of the Oman ophiolite: Implications for the origin of the oceanic lower crust, *Earth Planet. Sci. Lett.*, *146*, 475–488.

Kent, G. M., A. J. Harding, and J. A. Orcutt (1990), Evidence for a smaller magma chamber beneath the East Pacific Rise at 9°30′N, *Nature*, *344*, 650–653.

Kent, G. M., A. J. Harding, J. A. Orcutt, R. S. Detrick, J. C. Mutter, and P. Buhl (1994), Uniform accretion of oceanic crust south of the Garrett transform at 14°15′S on the East Pacific Rise, *J. Geophys. Res.*, *99*, 9097–9116.

Kent, G. M., I. I. Kim, A. J. Harding, R. S. Detrick, and J. A. Orcutt (1996), Suppression of sea-floor-scattered energy using a dip-moveout approach; application to the mid-ocean ridge environment, *Geophysics*, *61*(3), 821–834.

Kurras, G. J., D. J. Fornari, M. H. Edwards, M. R. Perfit, and M. C. Smith (2000), Volcanic morphology of the East Pacific Rise Crest 9°49′–52′: Implications for volcanic emplacement processes at fast-spreading mid-ocean ridges, *Mar. Geophys. Res.*, *21*, 23–41.

Lowenthal, D., L. Lu, R. Robertson, and J. Sherwood (1976), The wave equation applied to migration, *Geophys. Prospect.*, *24*, 380–399.

Ma, L. Y., and J. R. Cochran (1996), Transitions in axial morphology along the Southeast Indian Ridge, *J. Geophys. Res.*, *101*, 15,849–15,866.

Ma, L. Y., and J. R. Cochran (1997), Bathymetric roughness of the Southeast Indian Ridge; implications for crustal accretion at intermediate spreading rate mid-ocean ridges, *J. Geophys. Res.*, *102*, 17,697–17,711.

Macdonald, K. C., and P. J. Fox (1988), The axial summit graben and cross sectional shape of the East Pacific Rise as indicators of axial magma chambers and recent volcanic eruptions, *Earth Planet. Sci. Lett.*, *88*, 119–131.

Macdonald, K. C., P. J. Fox, R. T. Alexander, R. Pockalny, and P. Gente (1996), Volcanic growth faults and the origin of Pacific abyssal hills, *Nature*, *380*, 125–129.

McClain, J. S., J. A. Orcutt, and M. Burnett (1985), The East Pacific Rise in cross section: A seismic model, *J. Geophys. Res.*, *90*, 8627–8639.

McDonald, M. A., S. C. Webb, J. A. Hildebrand, B. D. Cornuelle, and C. G. Fox (1994), Seismic structure and anisotropy of the Juan de Fuca Ridge at 45°N, *J. Geophys. Res.*, *99*, 4857–4873.

Morton, J. L., N. H. Sleep, W. R. Normark, and D. H. Tompkins (1987), Structure of the southern Juan de Fuca Ridge from seismic reflection records, *J. Geophys. Res.*, *92*, 11,315–11,326.

Mutter, J. C., S. M. Carbotte, W. Su, L. Xu, P. Buhl, R. S. Detrick, G. M. Kent, J. A. Orcutt, and A. J. Harding (1995), Seismic images of active magma systems beneath the East Pacific Rise between 17°05′ and 17°35′S, *Science*, *268*, 391–395.

Nedimović, M. R., S. M. Carbotte, A. J. Harding, R. S. Detrick, J. P. Canales, J. B. Diebold, G. M. Kent, M. Tischer, and J. Babcock (2005), Frozen magma lenses below the oceanic crust, *Nature*, *436*, 1149–1152.

Normark, W. R., J. L. Morton, R. Koski, and D. A. Clague (1983), Active hydrothermal vents and sulfide deposits on the southern Juan de Fuca Ridge, *Geology*, *11*, 158–163.

Normark, W. R., et al. (1986), Submarine fissure eruptions and hydrothermal vents on the southern Juan de Fuca Ridge: Preliminary observations from the submersible *Alvin*, *Geology*, *14*, 823–827.

Pedersen, R. B., and H. Furnes (2001), Nd- and Pb-isotopic variations through the upper oceanic crust in DSDP/ODP Hole 504B, Costa Rica Rift, *Earth Planet. Sci. Lett.*, *189*, 221–235.

Perfit, M. R., and W. W. Chadwick (1998), Magmatism at mid-ocean ridges: Constraints from volcanological and geochemical investigations, in *Faulting and Magmatism at Mid-Ocean Ridges*, *Geophys. Monogr. Ser.*, vol. 106, edited by W. R. Buck et al., pp. 59–115, AGU, Washington, D. C.

Perfit, M. R., D. J. Fornari, M. C. Smith, J. F. Bender, C. H. Langmuir, and R. M. Haymon (1994), Small-scale spatial and temporal variations in mid-ocean ridge crest magmatic processes, *Geology*, *22*, 375–379.

Perfit, M. R., D. S. Stakes, M. A. Tivey, S. E. Kulp, W. I. Ridley, and T. M. Ramirez (2003), Magma genesis and crustal formation along the southern Juan de Fuca Ridge (JdFR): Results of fine-scale sampling and mapping, *Geophys. Res. Abstr.*, *5*, 07287.

Phipps Morgan, J., and Y. J. Chen (1993a), The genesis of oceanic crust: Magma injection, hydrothermal circulation, and crustal flow, *J. Geophys. Res.*, *98*, 6283–6297.

Phipps Morgan, J., and Y. J. Chen (1993b), Dependence of ridge-axis morphology on magma supply and spreading rate, *Nature*, *364*, 706–708.

Phipps Morgan, J., E. M. Parmentier, and J. Lin (1987), Mechanisms for the origin of mid-ocean ridge axial topography: Implications for the thermal and mechanical structure of accreting plate boundaries, *J. Geophys. Res.*, *92*, 12,823–12,836.

Purdy, G. M., J.-C. Sempéré, H. Schouten, D. L. DuBois, and R. Goldsmith (1990), Bathymetry of the Mid-Atlantic Ridge, 24°–31°N: A map series, *Mar. Geophys. Res.*, *12*, 247–252.

Purdy, G. M., L. S. L. Kong, G. L. Christeson, and S. C. Solomon (1992), Relationship between spreading rate and the seismic structure of mid-ocean ridges, *Nature*, *355*, 815–817.

Rubin, A. M. (1992), Dike-induced faulting and graben subsidence in volcanic rift zone, *J. Geophys. Res.*, *97*, 1839–1858.

Rubin, A. M., and D. D. Pollard (1988), Dike-induced faulting in rift zones of Iceland and Afar, *Geology*, *16*, 413–417.

Shah, A., and W. R. Buck (2001), Causes for axial high topography at mid-ocean ridges and the role of crustal thermal structure, *J. Geophys. Res.*, *106*, 30,865–30,879.

Sims, K. W. W., et al. (2003), Aberrant youth: Chemical and isotopic constraints on the origin of off-axis lavas from the East Pacific Rise, 9°–10°N, *Geochem. Geophys. Geosyst.*, *4*(10), 8621, doi:10.1029/2002GC000443.

Singh, S. C., G. M. Kent, J. S. Collier, A. J. Harding, and J. A. Orcutt (1998), Melt to mush variations in crustal magma properties along the ridge crest at the southern East Pacific Rise, *Nature*, *394*, 874–878.

Sinton, J. M., and R. S. Detrick (1992), Mid-ocean ridge magma chambers, *J. Geophys. Res.*, *97*, 197–216.

Sinton, J., R. Detrick, J. P. Canales, G. Ito, and M. Behn (2003), Morphology and segmentation of the western Galápagos Spreading Center, 90.5°–98°W: Plume-ridge interaction at an intermediate spreading ridge, *Geochem. Geophys. Geosyst.*, *4*(12), 8515, doi:10.1029/2003GC000609.

Small, C. (1994), A global analysis of mid-ocean ridge axial topography, *Geophys. J. Int.*, *116*, 64–84.

Smith, M. C., M. R. Perfit, and I. R. Jonasson (1994), Petrology and geochemistry of basalts from the southern Juan de Fuca Ridge: Controls on the spatial and temporal evolution of mid-ocean ridge basalt, *J. Geophys. Res.*, *99*, 4787–4812.

Smith, W. H. F., and P. Wessel (1990), Gridding with continuous curvature splines in tension, *Geophysics*, *55*, 293–305.

Sohn, R. A., and K. W. W. Sims (2005), Bending as a mechanism for triggering off-axis volcanism on the East Pacific Rise, *Geology*, *33*, 93–96.

Sohn, R. A., S. C. Webb, and J. A. Hildebrand (2004), Fine-scale seismic structure of the shallow volcanic crust on the East Pacific Rise at 9°50′N, *J. Geophys. Res.*, *109*, B12104, doi:10.1029/2004JB003152.

Soule, S. A., D. J. Fornari, M. R. Perfit, M. A. Tivey, W. I. Ridley, and H. Schouten (2005), Channelized lava flows at the East Pacific Rise crest 9°–10°N: The importance of off-axis lava transport in developing the architecture of young oceanic crust, *Geochem. Geophys. Geosyst.*, *6*, Q08005, doi:10.1029/2005GC000912.

Tivey, M. A. (1994), Fine-scale magnetic anomaly field over the southern Juan de Fuca Ridge: Axial magnetization low and implications for crustal structure, *J. Geophys. Res.*, *99*, 4833–4855.

Tivey, M. A., H. P. Johnson, C. Fleutelot, S. A. Hussenoeder, R. M. Lawrence, C. Waters, and B. Wooding (1998), Direct measurements of magnetic reversal polarity boundaries in a cross section of oceanic crust, *Geophys. Res. Lett.*, *25*(19), 3631–3634.

Tolstoy, M., A. J. Harding, and J. A. Orcutt (1993), Crustal thickness on the Mid-Atlantic Ridge: Bull's-eye gravity anomalies and focused accretion, *Science*, *262*, 726–729.

Vera, E. E., J. C. Mutter, P. Buhl, J. A. Orcutt, A. J. Harding, M. E. Kappus, R. S. Detrick, and T. M. Brocher (1990), The structure of 0- to 0.2-m.y.-old oceanic crust at 9°N on the East Pacific Rise from expanded spread profiles, *J. Geophys. Res.*, *95*, 15,529–15,556.

Wessel, P., and W. H. F. Smith (1995), New version of the generic mapping tools released, *Eos Trans. AGU*, *76*, 329.

Wilson, D. S. (1993), Confidence intervals for motion and deformation of the Juan de Fuca plate, *J. Geophys. Res.*, *98*, 16,053–16,071.

Yilmaz, Ö. (1987), *Seismic Data Processing*, *Investigations in Geophysics*, vol. 2, 526 pp., Soc. of Explor. Geophys., Tulsa, Okla.

Zelt, C. A., and R. B. Smith (1992), Seismic traveltime inversion for 2-D crustal velocity structure, *Geophys. J. Int.*, *108*, 16–34.

———————————

    J. Babcock, A. Harding, and G. M. Kent, Scripps Institution of Oceanography, IGPP-0225, University of California, San Diego, La Jolla, CA 92093-0225, USA.

    J. P. Canales and R. S. Detrick, Department of Geology and Geophysics, MS#24, Woods Hole Oceanographic Institution, 360 Woods Hole Rd., Woods Hole, MA 02543, USA. (jpcanales@whoi.edu)

    S. M. Carbotte, J. B. Diebold, and M. R. Nedimović, Lamont-Doherty Earth Observatory, Box 1000, Palisades, NY 10964, USA.

    E. van Ark, MIT-WHOI Joint Program, MS 22/Clark 242, 360 Woods Hole Road, Cambridge, MA 02543, USA.